NAVAL POSTGRADUATE SCHOOL
MONTEREY, CALIFORNIA

THESIS

MODIFICATION OF THE

NAVAL POSTGRADUATE SCHOOL

LIDAR SYSTEM

by

Murat Gunal

September 1995

Thesis Advisor :   Alfred W.Cooper

Approved for public release; distribution is unlimited

REPORT DOCUMENTATION PAGE	Form Approved OMB No. 0704

Public reporting burden for this collection of information is estimated to average 1 hour per response, including the time for reviewing instruction, searching existing data sources, gathering and maintaining the data needed, and completing and reviewing the collection of information. Send comments regarding this burden estimate or any other aspect of this collection of information, including suggestions for reducing this burden, to Washington headquarters Services, Directorate for Information Operations and Reports, 1215 Jefferson Davis Highway, Suite 1204, Arlington, VA 22202-4302, and to the Office of Management and Budget, Paperwork Reduction Project (0704-0188) Washington DC 20503.

1. AGENCY USE ONLY *(Leave blank)*	2. REPORT DATE September 1995	3. REPORT TYPE AND DATES COVERED Master's Thesis	
4. TITLE AND SUBTITLE **MODIFICATION OF THE NAVAL POSTGRADUATE SCHOOL LIDAR SYSTEM**		5. FUNDING NUMBERS	
6. AUTHOR(S) GUNAL, Murat			
7. PERFORMING ORGANIZATION NAME(S) AND ADDRESS(ES) Naval Postgraduate School Monterey CA 93943-5000		8. PERFORMING ORGANIZATION REPORT NUMBER	
9. SPONSORING/MONITORING AGENCY NAME(S) AND ADDRESS(ES) AEGIS Program Office PMS-400B		10. SPONSORING/MONITORING AGENCY REPORT NUMBER N0002495WRA0142	

11. SUPPLEMENTARY NOTES
   The views expressed in this thesis are those of the author and do not reflect the official policy or position of the Department of Defense or the U.S. Government.

12a. DISTRIBUTION/AVAILABILITY STATEMENT Approved for public release; distribution unlimited	12b. DISTRIBUTION CODE

13. ABSTRACT *(maximum 200 words)*
   Previous modifications were made to the Naval Postgraduate School (NPS) Lidar System to enable comparison of lidar returns with radiosonde vertical profiles. Inaccuracies due to flexing of the lidar mounting structure limited observation of correlation between lidar and balloon data. Reconstruction with a new telescope and integral mounting now provides stable overlap of laser illumination and receiver field-of-view while maintaining eye safety. This revised system permits more precise measurement of profile correlation. Both day and night lidar measurement series have been compared with concurrent radiosonde launches in the Monterey Bay area. Maximum ranges from clouds of greater than 3500 meters by day and greater than 5000 meters by night have been achieved. Within this range comparison can be made with moderate accuracy with the temperature and pressure profile boundary layer ceiling. Recommendations are made for future enhancement of sensitivity of correlation.

14. SUBJECT TERMS refraction, lidar, Nd:YAG, radiosonde, laser, lidar profile,			15. NUMBER OF PAGES 71
			16. PRICE CODE
17. SECURITY CLASSIFICATION OF REPORT Unclassified	18. SECURITY CLASSIFICATION OF THIS PAGE Unclassified	19. SECURITY CLASSIFICATION OF ABSTRACT Unclassified	20. LIMITATION OF ABSTRACT UL

N 7540-01-280-5500

Standard Form 298 (Rev. 2-89)
Prescribed by ANSI Std. 239-18 298-102

MODIFICATION OF THE NAVAL POSTGRADUATE SCHOOL LIDAR SYSTEM

Murat Gunal
Lieutenant Junior Grade, Turkish Navy
B.S., Turkish Naval Academy, 1989

Submitted in partial fulfillment of the
requirements for the degree of

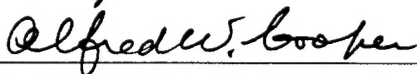## MASTER OF SCIENCE IN SYSTEMS ENGINEERING

from the

NAVAL POSTGRADUATE SCHOOL

September 1995

Author : _____
Murat Gunal

Approved by : _____
Alfred W. Cooper, Thesis Advisor

_____
K.L. Davidson, Second Reader

_____
Fred Levien, Chairman of Electronic Warfare Group

iii

iv

ABSTRACT

Previous modifications were made to the Naval Postgraduate School (NPS) Lidar System to enable comparison of lidar returns with radiosonde vertical profiles. Inaccuracies due to flexing of the lidar mounting structure limited observation of correlation between lidar and balloon data. Reconstruction with a new telescope and integral mounting now provides stable overlap of laser illumination and receiver field-of-view while maintaning eye safety. This revised system permits more precise measurement of profile correlation. Both day and night lidar measurement series have been compared with concurrent radiosonde launches in the Monterey Bay area. Maximum ranges from clouds of greater than 3500 meters by day and greater than 5000 meters by night have been achieved. Within this range comparison can be made with moderate accuracy with the temperature and pressure profile boundary layer ceiling. Recommendations are made for future enhancement of sensitivity of correlation.

TABLE OF CONTENTS

ACKNOWLEDGEMENT

I. INTRODUCTION

A. BACKGROUND

The Naval Postgraduate School LIDAR System was modified in previous years to provide information about atmospheric features such as changes in the temperature and humidity profiles of the atmosphere. Enhancement of the system was limited to the material and the instruments used in the design of the system. Since it was developed [Ref.1] to be an adjunct to the Naval Postgraduate School's Infrared Search and Target Designation System (NPS-IRSTD), some parts of the system were not designed or constructed to be consistent with the LIDAR objectives developed later. These disadvantages were eliminated in previous work [Ref.2] to the extent that material features allowed. The previous system used consisted of a laser transmitter which had a frequency-doubled Nd:YAG laser, a telescope which required later replacement to expand the beam to a level sufficient for meeting laser safety requirements, and a receiver employing a photomultiplier tube. The telescope structure was not sufficiently rigid to be stable in overlapping the laser illumination and the receiver field of view. The transmitter and the receiver parts were mounted on the telescope, which caused separate elements to vibrate or flex with respect to each other.Consequently, the telescope was replaced with a Celestron C14 cassegrain instrument. Use of the Celestron eliminated the misalignment problem due to flexing of the wooden structure of the previous telescope. Construction of a metal assembly carrying all the elements eliminated any problem that might have occurred because of any loose components.

B. RESEARCH OBJECTIVES

Detection of incoming threats by shipboard by radar (and to some extent infrared) sensors is hindered by propagation ducting effects due to atmospheric vertical profile features. Currently prediction of these effects relies on routine use of on-board radiosonde balloon launches, which is space and manpower intensive and may interfere with air operations. Eventual replacement of this procedure with a multifunction LIDAR system on major vessels is the objective of a large-scale development program. As an intermediate step it has been proposed that a small

1

low-power LIDAR system may be a feasible monitoring system to detect changes in the vertical profile and call for balloon launches only as needed, reducing the load on the ship crew.

The major objective of this research program is to evaluate the feasibility of this technique by comparison of back-scattered LIDAR returns from atmospheric boundary layer features with vertical profiles obtained with radiosondes. This objective included the analysis of the received signals to estimate the correlation of the lidar profiles and the radiosonde data.

In the redesign of the system one of the objectives was to keep the system within the limits of the eye safety requirements. So, the irradiance of the system was reduced by beam expansion using a Celestron 14 Telescope.

C. STRUCTURE

This thesis consists of six parts: Introduction, Atmospheric Parameters Affecting Electromagnetic Propagation, Lidar Theory, Experimental Arrangement, Experimental Procedure and Data Analysis, and Conclusions and Recommendations.

The first chapter, "Atmospheric Parameters Affecting Electromagnetic Propagation" explains the reasons to look for a way to define atmospheric features like humidity, temperature, density and some atmospheric occurrences such as trapping layers, and surface and elevated ducts.

The "Lidar Theory" chapter explains the fundamentals of the experiment, and leads to the definition of the data collection procedure, and the plans for analysis of the data. In this chapter, only those topics of lidar theory related to this thesis rather than general applications are included.

The "Experimental Arrangement" chapter explains the elements of the NPS lidar system and their properties. In case of a system inadequacy a recommendation for achievement of better performance is made. The limits of the system output power and of the received power are defined.

"Experimental Procedure and Data Analysis" is the main section addressing to what extent the use of a lidar system can avoid the necessity to launch a radiosonde balloon, and the

effectiveness of the analysed lidar data to define changes in atmospheric features. The approach to analysis of the correlation between the two system outputs is explained.

In the last chapter, " Conclusions and Recommendations ", the objectives are listed again and the effectiveness of the experiment to show the correlation between the lidar profiles and the radiosonde balloon profiles is criticized. Recommendations to enhance the system performance are also given.

II. ATMOSPHERIC PARAMETERS AFFECTING ELECTROMAGNETIC PROPAGATION

A. INTRODUCTION

The electromagnetic radio-frequency coverage pattern follows a "free space behavior " which is independent of the distance from the transmitting antenna along any radial, and varies with the angle from any radial. The earth and the atmosphere are the modifying mechanisms for this pattern. Some of the factors in these mechanism are as follows [Ref.3]:

1. Reflection from the earth's surface

2. Diffraction due to the earth's curvature

3. Ionospheric reflection

4. Atmospheric refraction

The last two factors are the subject of LIDAR studies.reasons for the comparison of lidar and radiosonde balloon measurements for evaluation of atmospheric features.

We can divide the atmosphere roughly into three layers for propagation characteristics as can be seen from Fig.2.1

1. Troposphere (lower than 10 km)

2. Stratosphere (between 10 km and 50 km)

3. Ionosphere (between 50 km and 600 km)

The troposphere has index of refraction properties that vary with altitude and weather conditions and is influential in bending electro magnetic (EM) waves. The stratosphere has a negligible effect on EM waves. The ionosphere can reflect signals which are low in frequency (caused by the ionized particles contained in the ionosphere). The earth alone can also reflect and diffract EM waves.

Electromagnetic energy can enter the shadow regions (regions behind obstacles or beyond the horizon) due to tropospheric refraction and ionospheric reflection. Refraction is the change in the direction of travel of radio waves due to a spatial change in the index of refraction.

5

The index of refraction [Ref.4] usually appears in the following form.

$$n = \frac{c}{v_p}$$ (2.1)

where   c is the speed of the light in a vacuum

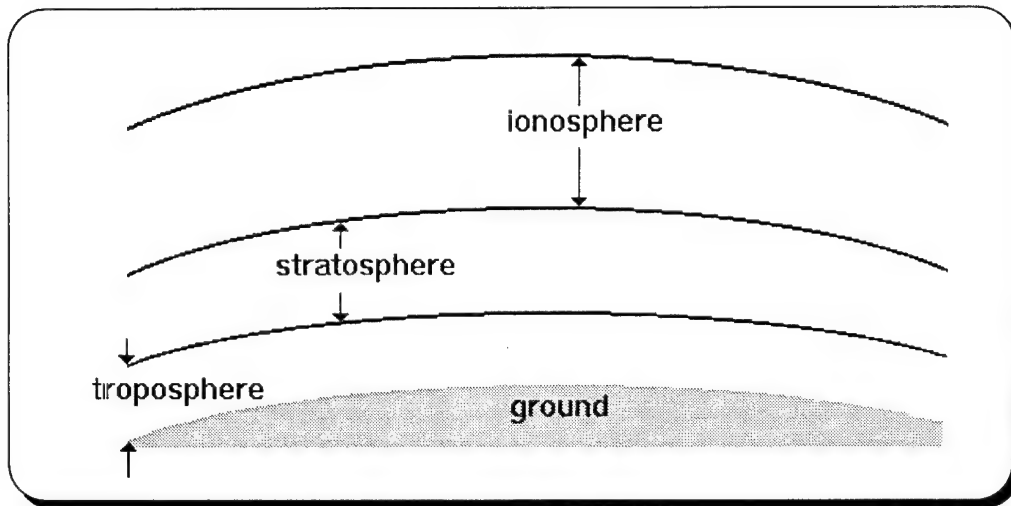v_p is the wave phase velocity in the medium

Figure 2.1. Atmospheric Layers

B. REFRACTIVE INDEX OF AIR

The refractive index of air for radio waves is very significant for determining the propagation ranges in the lower atmosphere. To see the effects of refractive index and refractivity, which is a term based on this index, it is necessary to consider some basic definitions and equations, which lead to the relations for electromagnetic propagation.

The index of refraction is found to be decreasing with increasing altitude for the average of many locations and long periods of time. The relation in Eq.2.1 shows that v_p increases as n decreases. Because of this relationship, the part of a transmitted wave that is at higher altitude (lower index) travels faster than the part that is closer to the ground (at higher index). Thus a

wave tends to bend downward (in the direction of higher index) under normal atmospheric conditions.

Under certain anomalous meteorological conditions, the radio energy may be confined to thin layers near the earth's surface with resultant abnormally high field strengths being observed beyond the normal radio horizon. At other times a transition layer between differing air masses will give rise to the reflection of radio wave energy.

Radio waves propagated through a medium with a varying index of refraction undergo both refractive bending and retardation of their velocity of propagation. These phenomena give rise to angle and range errors when a target is being tracked by a surface radar. The angular error is caused by the bending of the radar beam such that the wave front reflected from a target appears to be coming from a direction other than the target's true angular position in space; the range error is due to the increase in time necessary to travel over the curved path as compared to the straight-line path between target and receiver, and the variation in propagation velocity. For explaining the significant levels of errors (target angular error and target range error) due to this sample atmosphere refractive index profile, Fig. 2.2 and Fig. 2.3 will be helpful. [Ref.5].

In Fig. 2.2 it can be seen that as the target altitude increases or/and elevation angle of the transmitted beam decreases (as it becomes closer to the horizontal) angular error increases. This is because the upper part of a transmitted beam undergoes a different index of refractivity from the lower part. The reason for the range error in the second figure is the same. Because of the different indices of refractivity the propagation path changes to a curve rather than following a straight line. The relation between the altitude and angular error/range error is exponential.

The model used here is based upon a surface index of refraction and is referred to as the CRPL (National Bureau of Standards, Central Radio Propagation Laboratory) exponential atmosphere. This model is used to calculate the tropospheric angular and range errors presented in Fig.2.2 and Fig.2.3. The index of refraction "n" as a function of height "h" is given by [Ref.4]:

$$n(h) = 1.0 + 0.000313.e^{-0.00004385.h} \qquad (2.2)$$

where   h   is in feet for CRPL exponential atmosphere.

The angular error (Fig. 2.2) is the angle between the apparent ray path to the target from the radar and the straight-line path from the radar to the target. The range error (Fig. 2.3) is the apparent increas in range of the target caused by the wavefront traveling a curved path instead of a straight-line one.
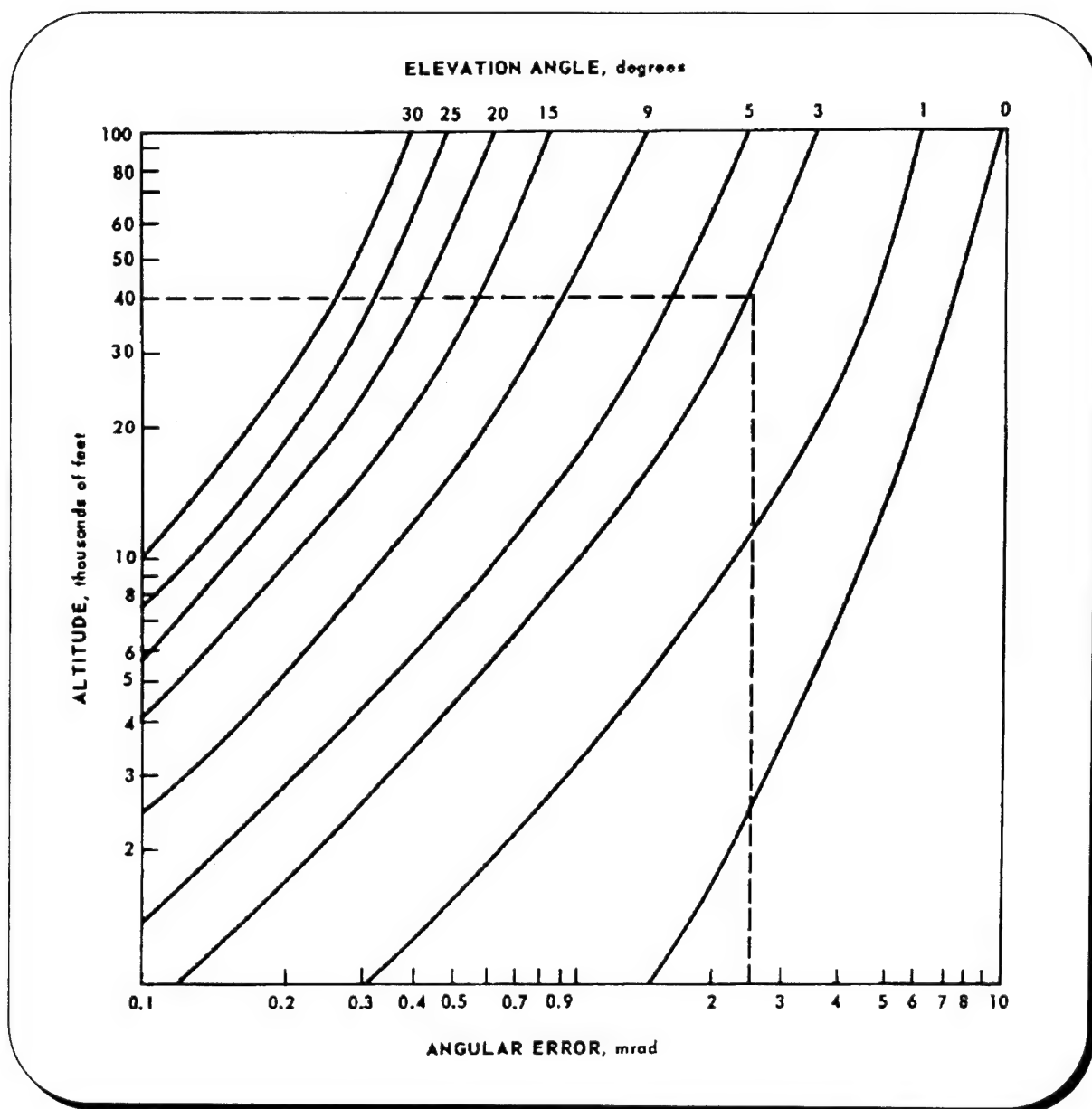

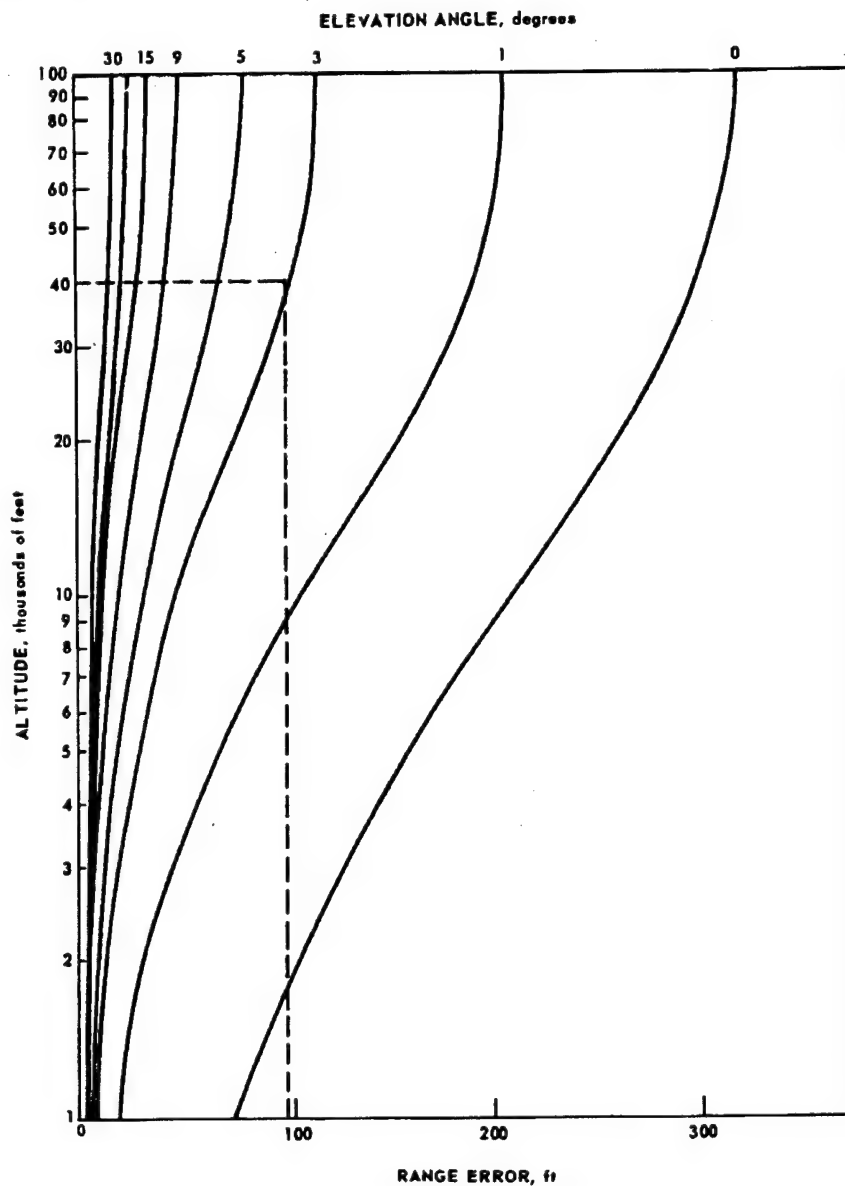Figure 2.2. Target Angular Error vs. Target Altitude [Ref.5]

Figure 2.3. Target Range Error vs. Target Altitude [Ref.5]

The errors that are apparent in these figures are known as bias errors since their magnitudes are calculable as long as the atmospheric refractive index is predicted to a high accuracy level. There are also some irregularities in the troposphere contributing to the

9

uncertainty in exact magnitudes of these errors. The Table 2.1 shows some of these irregularities and maximum rms values of the fluctuation of range and angle in the troposphere.

Type of weather	rms value of range error , ft	rms value of angle error,mrad
Heavy cumulus	2.0	0.7
Scattered cumulus	0.5	0.3
Small scattered cumulus	0.1	0.15
Clear moist air	0.02	0.07
Clear normal air	0.005	0.03
Clear dry air	0.001	0.015

Table 2.1. Tropospheric Irregularities Affecting Range/Angle Error [Ref.5]

It should be emphasized that the table above shows the biases for surface to air paths and does not take into account meteorological conditions at the time of the measurement. If a high degree of accuracy is desired modifications must be made to the reference atmosphere.

C. ANOMALOUS PROPAGATION

As explained above, the averaged values of refractive index around many places and during long time periods made it reasonable to use a standard refraction which changes according to Eq. 2.2. The model used in this equation gives us a good approximation unless we consider the factors in Table 2.1 and some other magnetic effects not to be mentioned in this thesis . Propagation which deviates from this approximation because of the factors mentioned above is called anomalous propagation. For the radar refraction pattern, we will consider subrefraction, superrefraction, and ducting, which all three are deviations from standard refraction. After browsing through these three conditions the ducting will be our main consideration.

10

1. Indices for Refractivity Profiles

A new model atmosphere must be considered to take into account the deviations from the standard atmosphere.This new model must involve the factors of temperature (T), water vapor partial pressure (e), and the pressure (P). Refraction through a medium of bound electrical charges depends upon the molecular types present and their density; for the atmosphere, refraction is primarily affected by vertical gradients of atmospheric temperature and water vapor partial pressure. These gradients are mainly important in the troposphere, in the lowest 10 km of the atmosphere.

The work that has been done in determining the atmospheric profiles showed that the main concern for refractivity is not its absolute value, but rather its gradient (dN/dz). The important point in this conclusion is that; dN/dz, which describes the refractivity, is controlled primarily by gradients of temperature and humidity since the dependance of the refractivity on these elements is much greater than its dependence on the pressure elements. The new model we have for refractivity is then [Ref.6]:

$$\frac{dN}{dz} = (-49km^{-1}) + (-1.4km.K^{-1})\frac{dT}{dz} + (4.5km.mb^{-1})\frac{de}{dz} \qquad (2.3)$$

If we know the temperature and humidity gradients in a region at a particular time, then we can easily obtain the refractivity profile by using the above formula.

2. Refractivity Gradient in Determining the Propagation Pattern

To define a radio wave propagation pattern in a region, the best approach is to find the refractivity pattern of the atmosphere where the propagation process will occur. For our purposes Eq. 2.3 is the convenient model to use. But, in other cases it is useful to use modified indices to depict specific refraction conditions such as "standard" and "trapping".

11

There is a well known relation [Ref.6] between the ray path radius of curvature (r) and index of refraction gradient in term of dN/dz:

$$r = \frac{-1}{(dn/dz)} = \frac{-10^6}{(dN/dz)} \tag{2.4}$$

A quantity defined as the " M-unit " is used in determining the presence and the absence of ducts (one of the concerns for the LIDAR applications). The M-unit is defined by [Ref.6]:

$$M = N + (157 km^{-1}).z \tag{2.5}$$

where N is the refractivity at any height

The required condition for a duct to be present in the refractivity profile is that dM/dz must be negative somewhere in the profile. The M-unit is also used to show the characteristics of ducts such as top and bottom of ducts

D. TRAPPING LAYERS AND DUCTS

1. Definition

The trapping layer can be defined from the refractivity profiles. It is the region on the profile where the N-gradient of refractivity is less than -157 km (dN/dz <-157) or the M-gradient is less than 0 (dM/dz <0). Physical interpretation of this is the region where the ray path will bend downward relative to the earth

A trapping layer can occur in two ways; either just above the surface, or in a way which does not extend down to the surface. The second occurrence is called the "elevated trapping layer".

A duct is also a similar layer which has its top always at the top of the trapping layer. The difference between the trapping layer and the duct comes from the fact that a duct can have its

12

bottom below the bottom of the trapping layer. Ducts can also have their bottom either on the surface or above the surface. The latter case is called the "elevated duct".

2. Determination of Trapping Layers and Ducts

It is mentioned in the previous sections that the M-profiles are used to define whether a trapping layer or duct exists in a region or not. In M-profiles the top of the duct and the trapping layer is the point where the slope changes from negative to positive. The bottom of the duct and the trapping layer may differ from each other. This can be seen from the following figure.
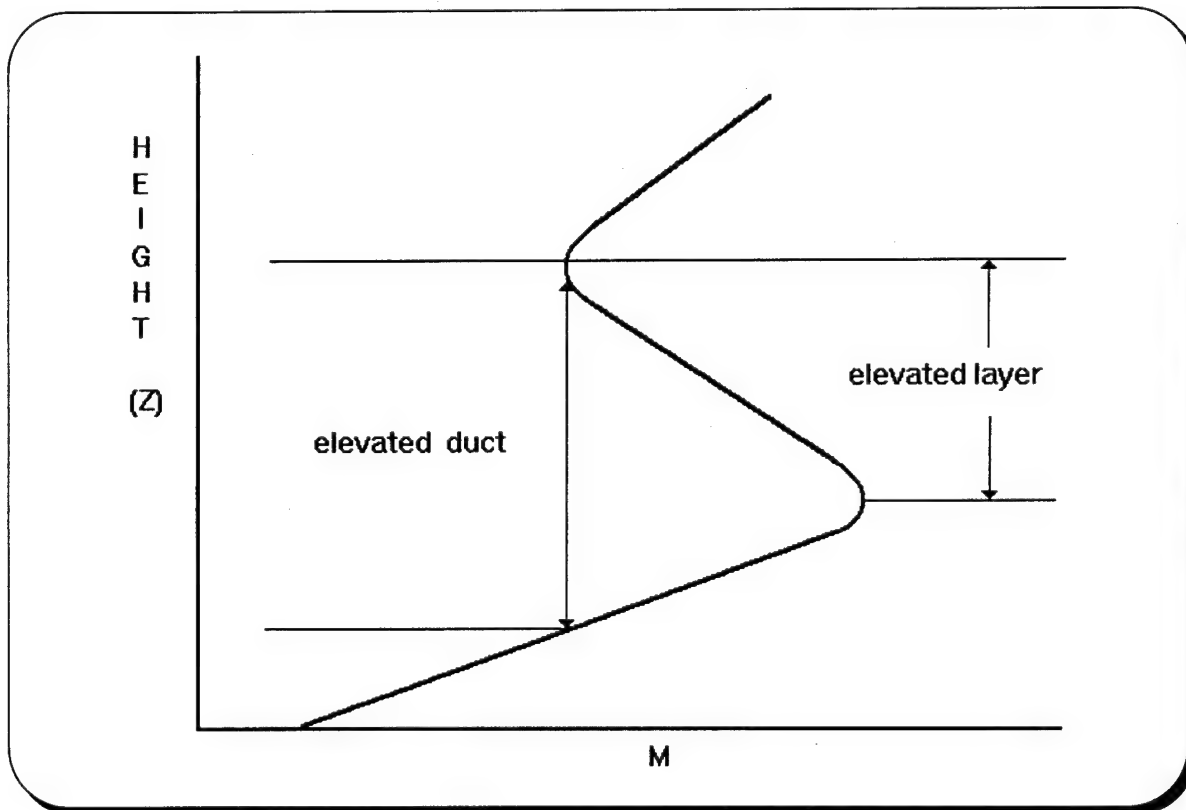
Figure 2.4. Trapping Layer and Duct Occurrence [Ref.6]

As can be seen from Fig.2.4 the trapping layer and duct are similar in concept and can be detected from the refractivity profiles. Negative values of the M-gradient are necessary for

13

formation of a trapping layer or duct. Then it is obvious from Eq.2.3 and Eq.2.5 that when the temperature increases rapidly with height and/or the humidity decreases rapidly with height a duct formation can be expected.

Two atmospheric regions are commonly the sources for duct and trapping layer formation (for negative M-profiles). These are either above a water surface, or at the top of a boundary-layer formed by the turbulence generated at the earth's surface. In the first situation, the humidity decreases rapidly with height and a surface-based duct is normally present.This kind of duct is called the "evaporation duct" and is typically 5-50 m deep. The second one is derived from large positive temperature gradients and large negative humidity gradients.

3. Ducting Effects in Propagation Patterns

Since the ducts are the regions in which refractivity changes with height, the propagation patterns are expected to change in the regions where ducting occurs. The changes in propagation patterns occur at the upper and lower boundaries of the ducts; The electromagnetic rays directed upward are reflected back and turn downward from the upper boundary of the duct. The downward directed rays turn upward from the lower boundary of the duct. [Fig.2.5]
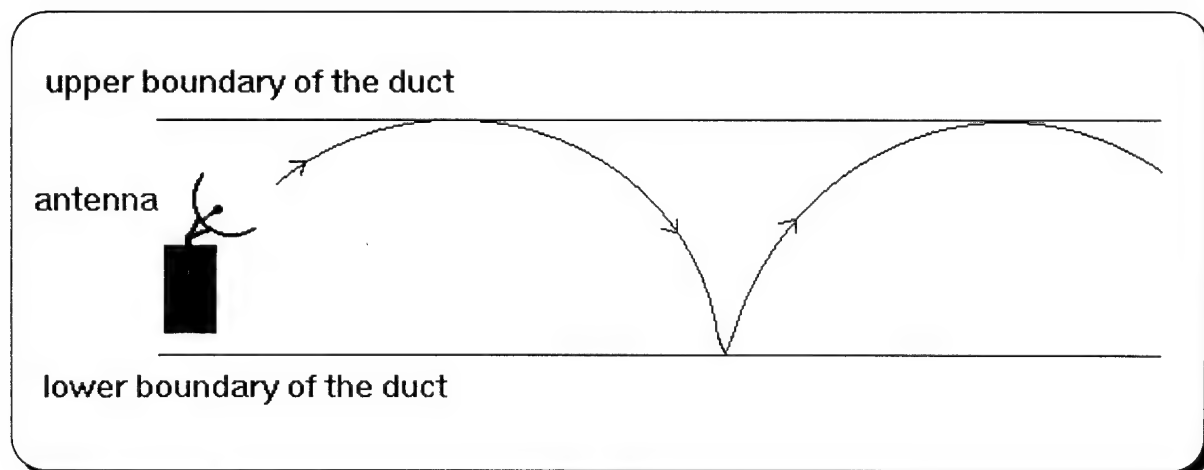

Figure 2.5. Ducting Effects in Propagation Patterns [Ref.4]

14

The type of the ducts (whether they are surface based or elevated) and their depth are closely related to the humidity and temperature gradients. So, they may exist in any region in the troposphere wherever the required humidity and the temperature gradients are found.

Ducting effects are very significant in calculating the efficiency of VHF propagation since they play a major role in extending the range of propagation or contrariwise creating some fadeout regions which degrade the performance of the system. Since it is a wide and complicated subject to explain all the refractivity patterns, only one situation, superrefraction, will be examined in this thesis to show the ducting effects on the propagation patterns.

The situation under discussion here is the ducting effect for radiation from a transmitter above a duct and a receiver within a duct. Some disruptions due to duct height and intensity may occur in communication systems. Whenever these disruptions occur, a high strength signal may be received beyond the horizon. Besides this, some deep, prolonged fadeouts can occur beyond the horizon or even in transmitter-to-receiver range. These fadeouts, usually called shadow zones, are shown in Fig.2.6 for the case defined above.
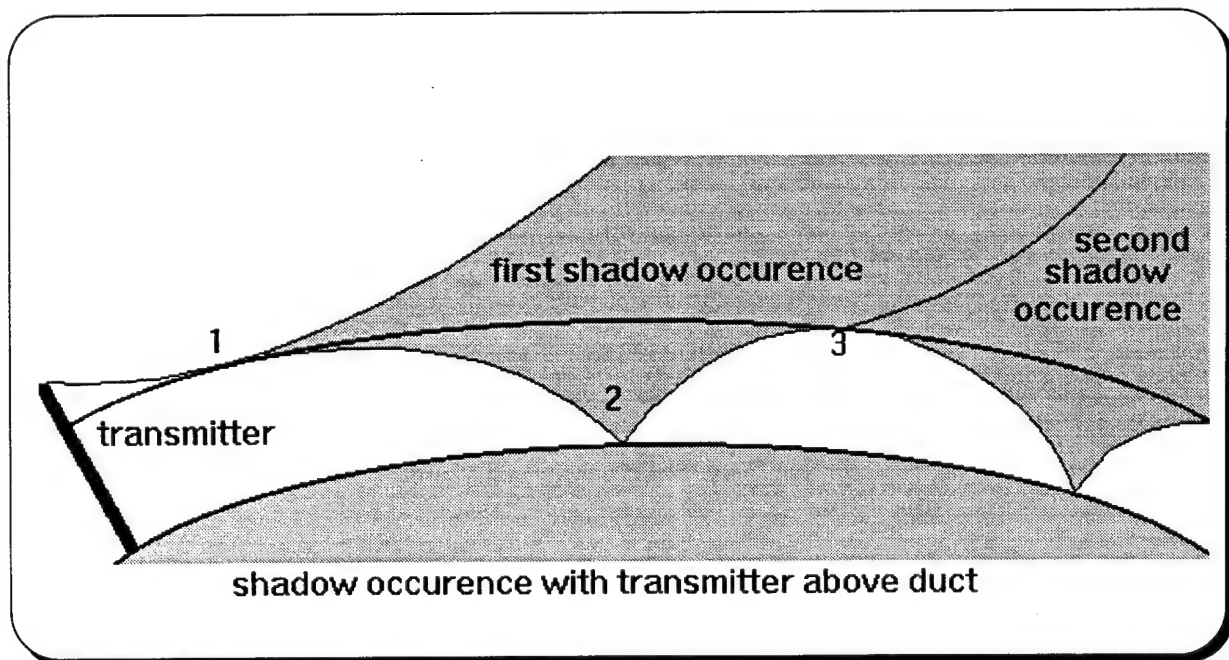

Figure 2.6. Shadow Zone and Fadeout Occurrence [Ref.7]

In Fig. 2.6 the radio ray at point 1 is divided into two parts; one is reflected above the top of the duct and the other is captured in the duct. The captured ray is reflected at point 2 and will split into two parts at point 3 again. In case of homogeneous surface duct the pattern from point 3 will be the same as from point 1 and also the rays will be symmetrical about point 2.

By examining this figure and the ones exhibiting ducting conditions and propagation patterns, one can estimate suitable values for location of the receiver; the receiver height, the location of the transmitter, etc. Actually, precise performance information requires scientific data such as the frequency, output power, and physical properties of the transmitter and the receiver, the ducting conditions in the region; temperature and the humidity gradients of the region and good statistical data about their variation according to time of the day (and sometimes long term seasonal changes).

It is obvious that the determination of atmospheric properties (for our purposes; ducting conditions) is very important in usage of the electromagnetic spectrum for both military and the civilian purposes. Hence, a great interest in finding efficient ways to detect these properties was born.

III. LIDAR THEORY

A. INTRODUCTION

There have been many previous attempts to measure atmospheric changes and properties with remote sensing devices. Light Detection and Ranging (LIDAR) has recently been found to be an efficient method in that area in a manner analogous to radar. The principle is to relate the return with time between the transmission of the laser pulse and the arrival of the scattered return signal. This basic relation gives us the range at which the scattering occurred. As the techniques of laser remote sensing devices advance, they can now be used for pollution monitoring, and evaluation of thermal, structural and dynamic properties of both the atmosphere and the hydrosphere, threshold detection of specific constituents, mapping of effluent plume dispersal and spectral fingerprinting of a specific target such as an oil slick.

There are many methods of remote-sensing using lasers, involving the phenomena of Rayleigh scattering, Mie scattering, Raman scattering, resonance scattering, fluorescence, absorption, and differential absorption and scattering (DAS). Among all these methods what we are interested in is Mie scattering, specifically at π radians.

Time series analysis of the Mie backscattered irradiance allows extraction of the range dependence of the scattering coefficient, and hence the visibility.

B. LIDAR SYSTEMS

The basic configuration for a lidar system consists of transmitter, receiver, and data processing system. Even though the number of the elements, system design, and the properties of the optics vary greatly between systems, their functions are usually the same.

In our model, the transmitter system consists of a laser and the transmitter optics which improve the beam collimation, provide spatial filtering, and block the transmission of any unwanted broadband radiation. We will see in Chapter IV that the Celestron 14

17

telescope collimates the laser beam, and the 532 nm reflective mirror after the expanding optics selectively reflects the 532 nm. beam and rejects the 1.06 micrometer laser beam.

The receiver is the component that gathers the radiation backscattered from the atmosphere or target and passes it through some optical filters to discriminate against the background radiation at other wavelengths. It consists of a telescope (Celestron 8) and three narrowband interference filters each centered at 532 nm and .88, .84, .9 nm wide (narrow band filters) in our model. In addition to the general elements of the receiver system, our receiver includes the amplifier unit and the auxiliary units including preampifier, logarithmic amplifier, voltage source, and high power voltage supply.

There are two standard configurations for lidar systems; bistatic and monostatic. In the bistatic case the transmitter and receiver systems are separated by a considerable distance. The monostatic configuration has the transmitter and receiver at the same location. There are two different monostatic configurations; coaxial and biaxial. In the coaxial system the axis of the laser beam is coincident with the axis of the receiver optics. The laser beam in a biaxial system enters the field of view of the receiver optics beyond some predetermined range. The biaxial configuration avoids the problem of near-field backscattered radiation saturating the photodetectors and puts no geometrical limit on maximum range.. The model we use is a monostatic configuration and is biaxial. The locations of the transmitter and receiver elements and the field-of-view configuration are shown in Fig. 3.1.

Backscattering to the receiver occurs only from the volume of overlap of the outgoing beam with the receiver field of view. As shown in Fig. 3.1 the angular field of view (FOV) of the receiver telescope (ϕ) is greater than the beam divergence of the laser through the transmitter telescope (θ). The "toe-in" inclination angle between the two telescope axes is then set to adjust the minimum distance for overlap of the receiver FOV and outgoing beam.
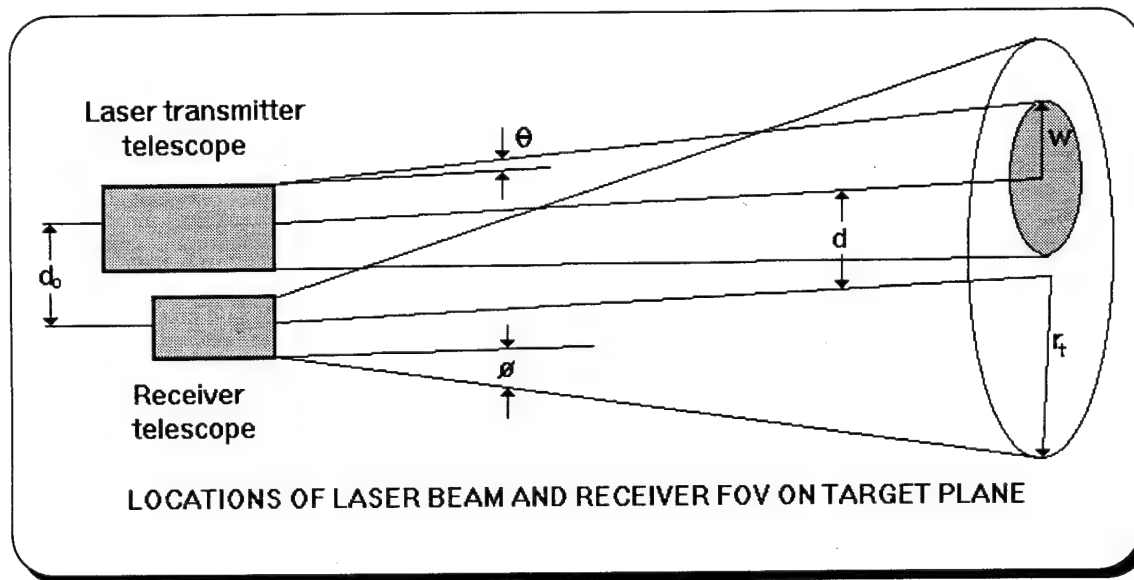
Figure 3.1. Field-of-View Configuration [Ref.8]

In Fig. 3.1 we can represent the separation of the telescope and laser axes in the target plane by use of the formula :

$$d = d_0 - R.\delta \qquad (3.1)$$

where d_0 is the separation of the axes at the lidar

δ is the inclination angle between the laser and telescope axes

R is the range where we examine the overlap area

There are three possible situations for the locations of the laser illumination and receiver fields of view:

1. The separation of the axes is too large ($> r_T + W$) and there is no overlap

2. The separation of the axes lies between the limits :
$$|r_T - W| < d < r_T + W$$

3. The separation of the axes is small and the area of laser illumination lies totally within the receiver field-of-view.

Our configuration shown in Fig. 3.1 is in the third group. During the system alignment tests we found the following values for the parameters above :

R = 260 ft. (The tests are done at this range for the laser beam and receiver field-of-view alignments)

19

d_0 = 14.75 inches

δ = 1.52 milliradians

θ = 0.208 milliradians

ϕ = 3.76 milliradians

W = 7.65 inches

r_T = 15.75 inches

The selection of detectors in lidar systems has great significance. It depends on the spectral response, quantum efficiency, frequency response, current gain, and dark current. As in our model, photomultipliers are preferred for wavelengths that lie between 200 nm and 1μm. They have the advantage of high gain and low noise. The performance of a photomultiplier is determined by the following specifications [Ref.8] :

1. The spectral response of the photocathode.

2. The dark-current characteristics of its photocathode.

3. The gain of the dynode chain.

4. The time dispersal effects of the electrons moving through the dynode chain.

5. The transit time of the electrons between the dynode and the anode.

The specifications of the photomultiplier tube can be found in Table 4.3.

The spectrum analyzer frequently included in the receiver assembly of lidar systems is for selecting a specific wavelength interval and rejecting all other emissions reaching the receiver. For remote sensing this element may consist of absorption filters, interferometric elements, and dispersive systems. The NPS LIDAR uses a simple set of three 532 nm. narrowband interference filters to reject background radiation at all wavelengths other than that of the laser.

Lasers used in lidar systems are desired to have the capability of emitting pulses of optical energy that possess very high peak power, narrow bandwidth, short duration and low degree of divergence. The peak power in the Naval Postgraduate School LIDAR system is not sufficient to reach ranges greater than 6 km due to the imposed condition of satisfying the eye safety requirements. The laser we used is Nd:YAG with the specifications defined in Table 4.1.

LIDAR return signals appear as amplified current or voltage output from the optical detector, which is triggered from the laser pulse output, and hence show relative backscatter as a function of time lapse. The range to the point of scattering is proportional

20

to the time lapse after pulse emission. The scattering may be from clear air (molecules), from aerosol particles or clouds, or from solid targets. The signals are displayed versus time on the output screen of a wide-band oscilloscope. Figure 3.2 shows a typical clear air return displayed on a Hewlett-Packard HP 5411D digitizing oscilloscope which has a sampling rate of 1 gigasample. The return signal is represented by a negative peak due to the amplifier coupling. The scatter of the digitization points represents the noise in the signal. The time base scale in microseconds can be converted into lapsed time by superposition of the trigger signal, and thus into range.
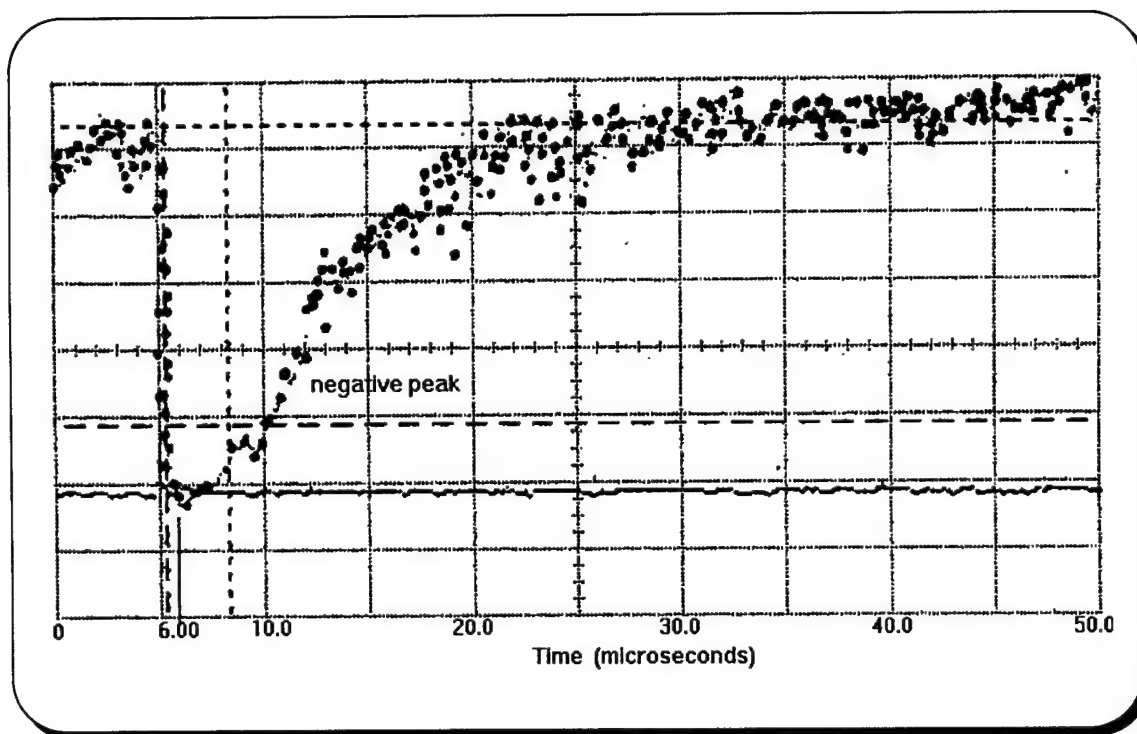

Figure 3.2. Typical Clear Air Back-scatter Signal Displayed on HP 5411D Oscilloscope

This is a typical backscatter return. The distortion of the signal (fluctuations) is due to the noise. Types of noise that can exist in a lidar system are [Ref.8] :

1. Noise in signal (quantum noise) : This arises from statistical fluctuations in the signal current. This is generated from the statistical fluctuations in the generation of the secondary electrons at the dynodes in the photomultiplier tube. The factors determining the

noise associated with a photomultiplier tube are the characteristics of the photocathode, the operating gain, and how this particular photomultiplier has been used before.

2. Background-radiation noise : Due both to statistical fluctuations of the background radiation and to the fluctuations caused by the current generated by the background radiation. The spectral radiance of the clear daytime sky peaks in the visible (due to the scattered solar radiation). This is observed in lidar systems aimed at the sky, and is found to be the most serious problem in our daytime sky-aimed lidar measurements. The level of the background radiation noise prevents weak signals being revealed since the spectral radiance of the clear daytime sky peaks in the visible, and is partially in-band to our system which works at the visible wavelength of 532 nm.

3. Dark-current noise : Due to thermal generation of current carriers in the absence of an optical signal.

4. Thermal (Johnson, Nyquist) : Due to thermal agitation of current carriers in resistive circuit elements.

The first three are different forms of shot noise, proportional to the total current flowing in the detector. This is the noise resulting from the statistical generation of electrons by the cathode. The rms value of the shot noise is given by [Ref.9] :

$$i_N = \sqrt{2.e.(i_s + i_d + i_b).\Delta f.G^2}$$
(3.2)

where i_s is the current on the cathode from the backscattered signal
i_d is the dark current. It arises from thermal and field-emission processes. This
   noise is present even in the absence of light.
i_b is the current generated by the background radiation
Δf is the noise (amplifier) bandwidth
 G is the detector internal gain factor

The background current can be written in the form:

$$\overline{i_b} = \frac{\lambda.e.\eta(\lambda).E_b(\lambda)}{h.c.\tau_d}$$
(3.3)

22

where λ is the wavelength of the background radiation

      $\eta(\lambda)$ is the quantum efficiency of the photomultiplier tube

      $E_b(\lambda)$ is the background radiative energy arising from natural sources (Joules.nm^{-1})

      e   is the electron charge

      c   is the speed of light

      h   is Planck's constant

      τ_d is the detection interval which is determined by the response time of the PMT.

In this equation the increment of the radiative energy from natural sources reaching the receiver optics and accepted through its receiving optical bandwidth in the detection time τ_d is expressed as below [Ref. 8]

$$E_b(\lambda) = \int_{\Delta\lambda_0} S_b(\lambda').\xi(\lambda').\Omega_0.A_o.\tau_d.d\lambda' \qquad (3.4)$$

where $S_b(\lambda')$ is the spectral radiance of the sky background (W.cm^{-2}.nm^{-1}.sr^{-1})

      $\xi(\lambda')$ is the receiver-system transmission efficiency at the wavelength λ' and includes the influence of any spectrally selecting components such as lenses and filters. These components are narrowband filters in our system and they are centered at 532 nm.

      $\Delta\lambda_0$ is the spectral window of the receiver system. Again, the filters have a significant effect on the spectral window of the receiver system. Transmittance curves of the three filters used in the receiver system are given in Fig. 3.2.

      A_0 is the effective aperture

      Ω_0 is acceptance solid angle

We try to keep the receiver system optical bandwidth, $\Delta\lambda_0$, as small as possible and compatible with the wavelength of 532 nm. Since we achieve this with filters which have the characteristic curves given in Fig. 3.2, we can write the radiative energy as :

$$E_b(\lambda) = S_b(\lambda).\Omega_0.A_0.\tau_d.\kappa_0(\lambda) \qquad (3.5)$$

where λ is the center wavelength of the radiation (532 nm for our system)

$\kappa_0(\lambda)$ is the filter function of the receiver system (effective receiver bandwidth at unit transmission efficiency) which is found by integrating the receiver system transmission efficiency over the spectral window of the system.

So, we can write Eq. 3.3 in the following form which includes the specifications of the receiver and of the optics inside it :

$$\overline{i_b} = \frac{\lambda.e.\eta(\lambda).S_b(\lambda)\Omega_0.A_0.\kappa_0(\lambda)}{h.c} \qquad (3.6)$$

The fourth class of noise is thermal noise or commonly called Johnson noise. This noise is generated by the thermal excitation in resistive circuits. Its RMS value is given by the following equation :

$$i_{rms_j} = \sqrt{\frac{4.k.T.\Delta f}{R}} \qquad (3.7)$$

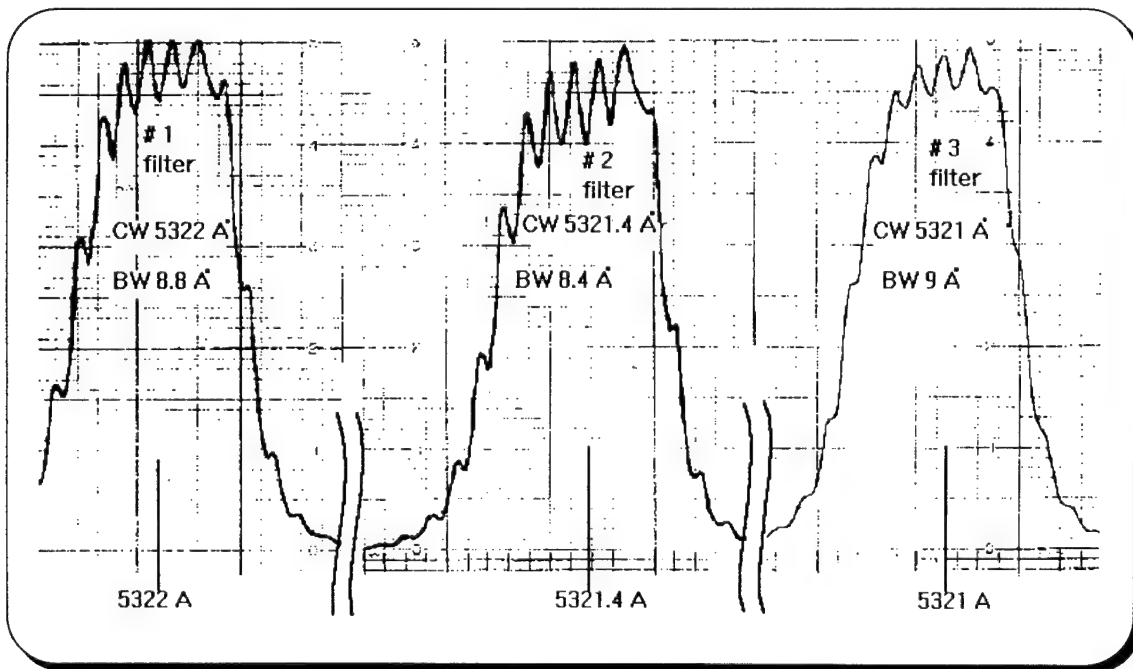where $\Delta f \equiv \frac{1}{2.\tau_d}$ is the photodetection bandwidth.

Figure 3.3. Spectral Transmission Function for Narrow Band Filters

24

In our case the dominant noise factor is shot noise rather than thermal noise. Then, we can express the signal-to-noise ratio of our system as:

$$SNR = \frac{i_s}{[2.e.\Delta f.(i_s+i_b+i_d)]^{1/2}}$$ (3.8)

Since R is large enough in $\frac{4.k.T.\Delta f}{R}$ we neglected the Johnson noise.

As was the case in our experiment, the range and detection threshold of a lidar is usually limited by the presence of background luminescence at the same wavelength as the signal. This may result from scattered solar radiation or from laser-induced fluorescence. A significant part of this broadband radiation can be reduced to negligible levels by use of narrowband filters. This method is applied in our system. By use of filtering through narrowband filters we tried to reduce the level of background luminescence, especially for daytime operations.

It is also possible for near-field backscattered laser radiation to saturate the photodetector, which happened during our experiments and restricted the near field measurements of the system. The restriction in our system is that the saturation region extends to 1 microsecond after the trigger signal, which corresponds to a region of 150 meters blind to small signals.

C.   DAY LIGHT LIDAR OPERATION

In day light lidar operation, the background radiation constitutes the dominant source of noise. Therefore, we write Eq. 3.8 again in the following form :

$$SNR= \frac{i_s}{[2.e.\overline{i_b}.\Delta f]^{1/2}}$$ (3.9)

If we equate this to 1 and use Eq. 3.3 to replace $\overline{i_b}$ we will have a new equation which we can equate with :

$$i_s= \frac{\lambda.e.\eta(\lambda).P(r)}{h.c}$$ (3.10)

25

This gives for the power equation :

$$P(r) = \sqrt{\frac{2.h.c.\Delta\lambda.S_b(\lambda).\tau_0(\lambda).\Omega_0.A_0.\Delta f}{\lambda.\eta(\lambda)}} \qquad (3.11)$$

If we substitute this in the basic lidar equation, [Ref.7] we find :

$$P(r) = P_0\frac{A_0}{R^2}.\xi(\lambda).\xi(R).\beta(\lambda,R).\frac{(c\tau)}{2}.e^{-2\int_0^R \kappa(\lambda,R).dR} \qquad (3.12)$$

where P(r)   is the energy received by the detector

P_0 is the initial energy transmitted by the laser

A_0 is the effective aperture of the receiver optics

R   is the range from the detector

$\xi(\lambda)$ is the transmission efficiency of the receiver optics at wavelength λ. In the derivation of Eq. 3.13, the representation $\tau_0(\lambda)$ was used for transmission efficiency

$\xi(R)$ is the geometric form factor. It splits into two terms. The first term is the overlap function which has three possible cases; no overlap, complete overlap (as in our system), and partial overlap. The second term expresses the reflected lidar signal from the near field not being in the focal plane of the receiver telescope.

$\beta(r)$ is the atmospheric volume backscatter coefficient at range r (meters^{-1}. str^{-1})

τ is the laser pulse width

$\kappa(\lambda,R)$ is the attenuation coefficient of the atmosphere for wavelength λ.(meters^{-1})

We can solve Eq. 3.12 for maximum theoretical range as :

$$r_{max} = \sqrt{\frac{P_0.\tau.\beta(r).\sqrt{c.A_0.\tau_0(\lambda).\lambda.\eta(\lambda)}.e^{\left[-2\int_0^{r_{max}} \sigma(r').dr'\right]}}{\sqrt{8.h.\Delta\lambda.S_b(\lambda).\Omega_0.\Delta f}}} \qquad (3.13)$$

where r_{max} is the maximum range of the lidar system (meters)

P_0 is the transmitted power (watts)

26

τ is the laser pulse width (seconds)

c   is the speed of light (meters per second)

A_0 is the effective aperture of the receiver

λ is wavelength of the background radiation which is matched to the receiver bandwidth after the filters (meters)

$\eta(\lambda)$ is the quantum efficiency of the photomultiplier tube

$\sigma(r)$ is the atmospheric extinction coefficient (meters^{-1})

h   is Planck's constant (watts.seconds^2)

$\Delta\lambda$ is the narrow band filter width (microns)

$S_b(\lambda)$ is the spectral radiance of the background (watts.meters^{-2}.str^{-1}.microns^{-1})

$\tau_0(\lambda)$ is the receiver optics transmission efficiency at wavelength λ.

D.   NIGHT TIME LIDAR OPERATION

In night time lidar operation, the background noise falls to the minimum level and the signal current becomes the dominant factor. For this reason many systems -especially the ones with weak noise filtering, vulnerable to radiation from natural sources such as the sun-have better performance during night time operations. SNR in this case is :

$$SNR = \frac{i_s}{[2.e.\overline{i_s}.\Delta f]^{1/2}} \qquad (3.14)$$

Here the laser pulse width is between 40 and 50 nanoseconds and the response of the R1913 type photomultiplier is given by its anode rise time plus electron transit time as 1.0 nanosecond at 2000 Vdc. This means that the response time of the photomultiplier is much smaller than the laser pulse width. Hence, we can assume that the signal current i_s is equal to the average value $\overline{i_s}$. This shortens the Eq. 3.14 into the following form :

$$SNR = \left[\frac{i_s}{2.e.\Delta f} \right]^{1/2} = \left[\frac{\lambda.\eta(\lambda).P(r)}{2.h.c.\Delta f} \right]^{1/2} \qquad (3.15)$$

Equating this value of SNR to unity, we find the minimum power that can be received as:

$$P(r) = \frac{2.h.c.\Delta f}{\lambda.\eta(\lambda)} \qquad (3.16)$$

This is substituted into Eq. 3.12 again to find maximum night time operation range:

$$r_{max} = \sqrt{\frac{P_0.\tau.\beta(r).\tau_0(\lambda).A_0.\lambda.\eta(\lambda).e^{\left[-2\int_0^{r_{max}} \sigma(r').dr'\right]}}{4.h.\Delta f}} \qquad (3.17)$$

where the parameters are same as in Eq. 3.13.

We can estimate the maximum day time and night time ranges by using Eq.3.13 and Eq.3.17. The results can be compared to the actual lidar ranges that the system received the signals from.

IV. EXPERIMENTAL ARRANGEMENT

A. INTRODUCTION

The overall design consists of three parts; the transmitter system, the receiver system, and the data processing system. The system is mounted on a Pelco PT2000 Pan and Tilt Unit. This unit consists of the C14 Declination Clamps and the Control Unit which has the pan and tilt angle/speed controls on it. The declining system and the limitations were kept the same as in the last year's experiment. The limitations are $\pm 90^o$ in elevation and 0° to 355° in azimuth. The changes made from the previous system are explained in the transmitter unit and receiver unit sections of this chapter. The modifications of both the receiver and the laser transmitter helped improve overall performance of the system.
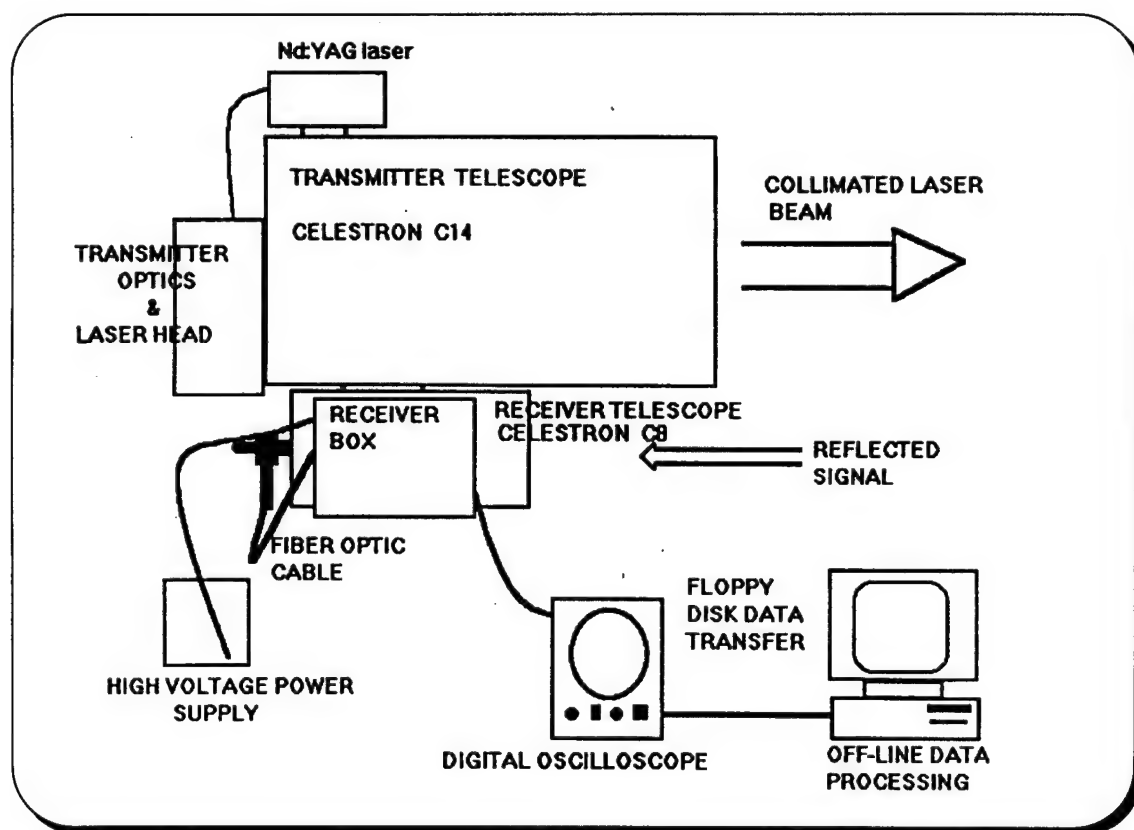
The system block diagram is as follows:

Figure 4.1. Block Diagram of the Lidar System

The elements of this system are discussed separately below.

29

B. TRANSMITTER ASSEMBLY

1. Laser

The laser used in the transmitter is the same frequency-doubled Nd:YAG medical laser used previously which radiates at the wavelengths 532 nanometers and 1.06 micrometers. The laser system consists of the laser power supply and the laser head. Together these form the model MK 100 Nd:YAG laser system manufactured by Kigre Incorporated.

The power supply unit contains the control section for the laser. The specifications of the laser are as follows

CHARACTERISTICS	VALUE	
maximum energy output	mean = 9.126 joules	
	Std. Dev. = 1.587	
beam diameter	±0.2mm.	
half angle beam divergence	0.165 ± 0.001 milliradians	
energies available	laser settings	real values
	0.9	.47
	1.2	.68
	1.8	.65
	2.5	.912
	4.0	.87
	5.0	1.22
	7.5	1.36
	10.0	2.06

Table 4.1. Laser Specifications [Ref.2]

The number of pulses per shot is selected in steps (starting from 1 ending at 5) from the laser power supply and the laser output pulse energy has eight different selectable settings.

The laser head is equipped with three filters which reduce the output energy by different selectable ratios. These are neutral density filters made from glass of types NG 11,

30

NG 4, and NG 9. The thickness of the filter glasses varies between 0.8 mm and 4.5 mm. Thus by using these three glass types, the values of the spectral optical density at the 546 nm wavelength (designated as D(546 nm)) can be adjusted between 0.15 and 5, and the spectral transmission at 546 nm (designated as τ (546 nm)) can be adjusted between 0.78 and 1×10^{-5}. Kigre Corporation reports that these measurements are valid at 532nm.

The laser wavelengths produced by the laser head are 532 nm and 1.06 μm, of which the latter is eliminated by a beam splitter after the first beam expander. Therefore the optics that are used in the following parts, such as narrowband filters, are chosen for the specific (532 nm) wavelength.

The laser output power was found to show major variability and average power lower than reported by Kigre Corporation in 1992.

2. Transmitter Telescope

The transmitter telescope used in the previous experiment was a Dall-Kirkham, Cassegrain type instrument. This was replaced due to the lack of the rigid structure which is needed to keep the receiver and transmitter parts aligned. Objective mirror deterioration as noted in Ref.8 made it necessary to replace the telescope.

The new telescope used is a Cassegrain type Celestron model C14. The collimation adjustment of the telescope is accomplished by two different systems. The primary focusing is by adjusting screws on the secondary housing; these should not be changed unless major realignment is necessary. The secondary, routine, adjustment is with the two screws and an adjustment knob on the rear face of the telescope.

The laser beam has a half angle beam divergence of 0.417 milliradians after the collimation by the telescope.

The general specifications of the telescope are as in Table 4.2 [Ref.11]:

3. Laser Optics

The optics used in the previous system did not allow enough power to pass through the telescope mount. The reason for that was misalignment of the optics with the mounting

31

of the telescope. Consequently, the optics in the transmitter box were redesigned. The beam expander before the first mirror (beam splitter) was adjusted again and the lens after the mirror was relocated. The laser beam through this lens was originally 6 mm below the input to the transmitter telescope. To correct this, all of the optics and the laser head were raised by 6mm by mounting them on an aluminum plate. After these modifications to the previous system an unobstructed signal was detected through the output of the transmitter box into the telescope. The new location of the optics in the transmitter box is as in Fig. 4.2.

manufactured by	Celestron International
clear aperture	14 inches (350 mm)
optical design	Schmidt-Cassegrain catadioptric; diffraction limited
focal ratio	f / 11
focal length	154 inches (3,910 mm)
primary mirror:	
figure	spherical
diameter	14.25 inches (361.9 mm) clear ap.
f / ratio	f / 2.14
radius of curvature	60 inches (1.524 meters)
secondary mirror :	
figure	spherical
diameter	3.50 inches (88.9 mm)
radius of curvature	17.6 inches (447 mm)
amplification ratio	5.14
central obstruction	4.5 inches (10 % by area or 32 % by diameter)

Table 4.2. Transmitter Telescope Specifications

The time reference trigger signal was generated from pulse radiation escaping through the rear mirror of the laser, fed through a fiber-optic cable to a pin diode detector on the outside of the box. The coupling from the laser to the fiber optics input, which had proved unreliable, was replaced with a wider mirror with increased acceptance angle to improve reproducibility.

The trigger cable should be replaced in the upcoming experiments to eliminate sharp bends in the cable. This is expected to increase the level of the trigger signal by decreasing losses.
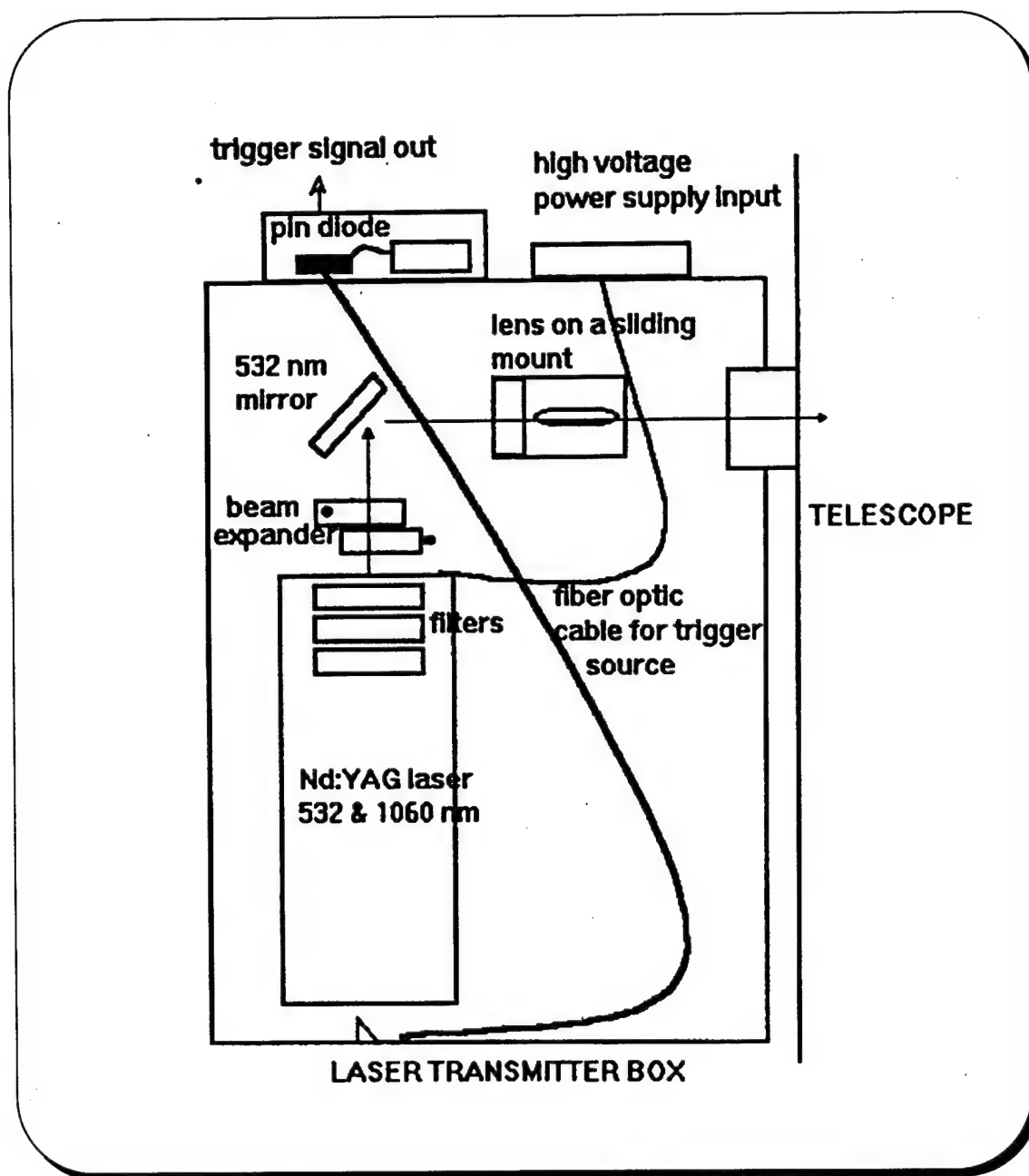

Figure 4.2. Block Diagram of the Laser Transmitter Box

C. RECEIVER ASSEMBLY

1. Receiver Telescope

The telescope used in the previous measurements was a Cassegrain type telescope with a focal length of 750 mm and a f-number of 6. This telescope was changed to provide a bigger receiver area and better efficiency. The new receiver telescope is a Celestron C8 type telescope which has a focal length of 2032mm (f/10). The large aperture of the C8 allows light gathering power 843 times that of human eye.

The optical output of the previous telescope was connected to the receiver box directly via a connection box and an aluminum pipe containing transfer optics. The connection box in the previous system contained a 532 nm selective mirror which redirected the beam $90°$ downwards toward the receiver box and the aluminum pipe contained a f/3.5 lens and a 10 nm narrowband optical filter. This configuration was changed due to the new locations of the elements. The direct optical aluminum light guide in the new system is not directly connected to the receiver box; the optical signal passing through it is focused into a fiber optic cable connecting to the photomultiplier box at the other end. This allows for later modification of the optics inside the aluminum light pipe more easily and without harming the photomultiplier box. Another advantage of the new setup is that it gives the enough space to add/replace the optics with longer focal lengths. The setup of the optics between the 532 nm selective mirror and the fiber cable is shown in Fig. 4.3.

2. Receiver Box

The units in the receiver box are the voltage source, the photomultiplier tube (PMT) box (with preamplifier in it), the logarithmic amplifier, the mixer, and power supply. The power supply inside the box is not currently in use. Instead, we have a new high voltage power supply which is mounted separately from the system.
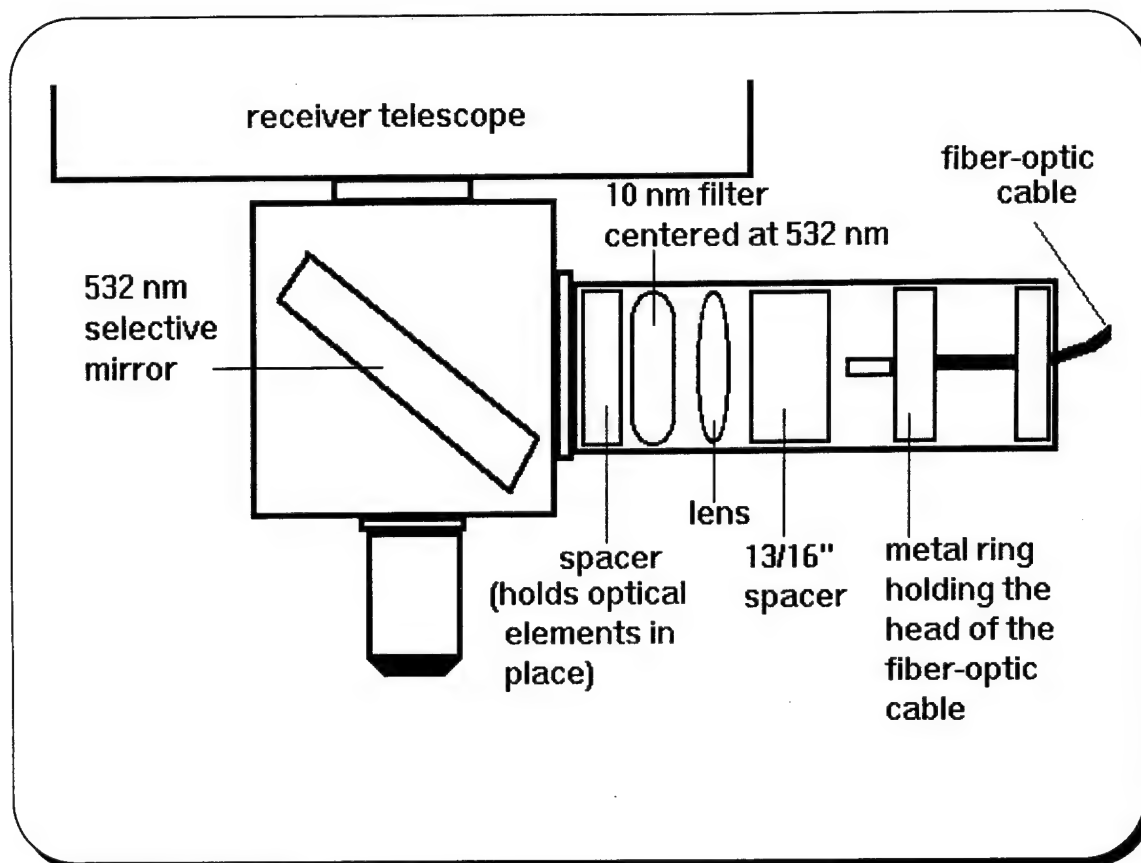
34

Figure 4.3. Receiver Telescope to PMT Connection

The PMT entrance of the receiver box is connected to the receiver telescope via fiber optic cable. This side of the box has a HMV type connector on it for high voltage power supply connection. The other end of the receiver box has a socket for the voltage source of the receiver elements. This face carries the logarithmic amplifier and DC output connections (coming from the mixer) on it. [Fig. 4.4]

The voltage source supplies -18, -6, +6, -5, +5 volts to the preamplifier and logarithmic amplifier stages. Although the noise in the voltage source is at a low level, the performance of the overall system can be increased if it is examined and reduced to a lower level. Fig. 4.4 shows the circuit diagram with the voltage source (previously used) in the receiver box.

The PMT box contains two elements; an R1913 photomultiplier and a preamplifier unit. The specifications of the photomultiplier are given in Table 4.3. [Ref.12]
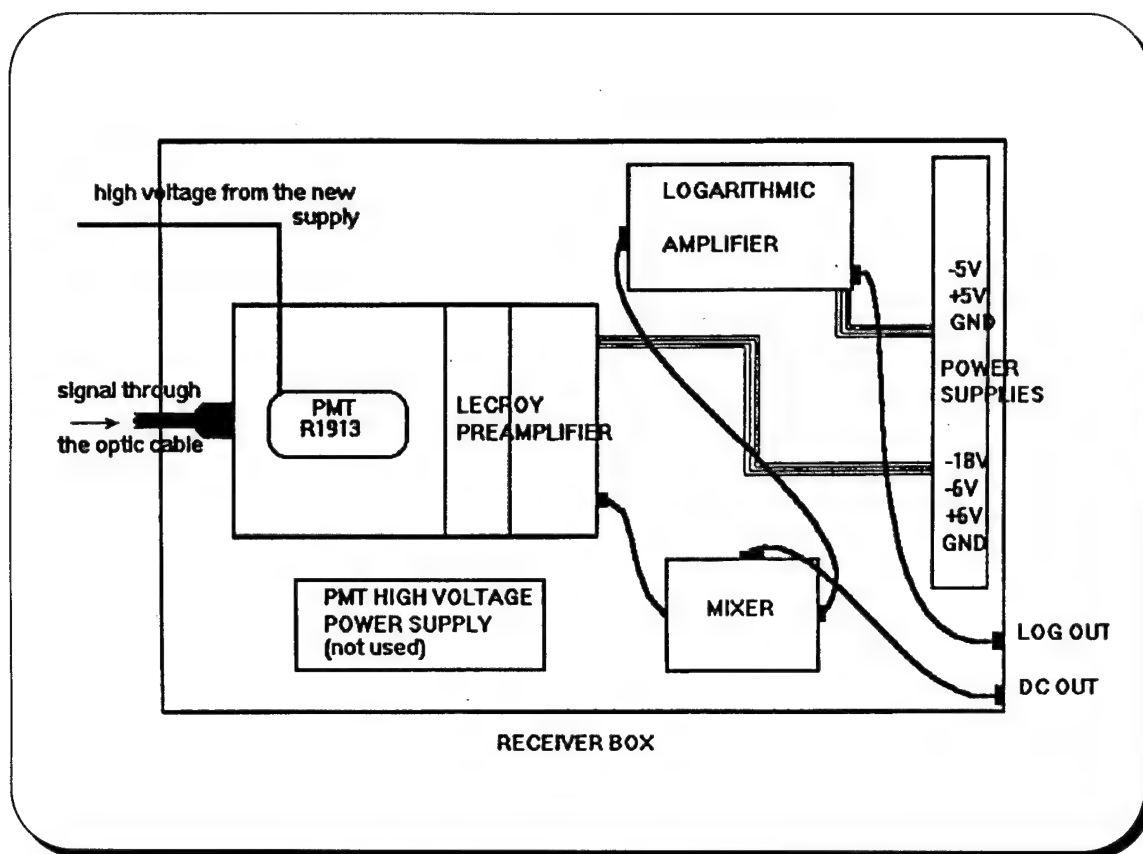
Figure 4.4. Block Diagram of the Receiver Box

The preamplifier used in the receiver box is a Le Croy, Model VV100B wideband pulse amplifier. It was DC coupled to the PMT to minimize the capacitance. This was done

cathode sensitivity	55 milliamperes / watt (532 nanometers)
current amplification	3.0×10^3
rise time	1.0 nanoseconds (2000 V DC)
anode dark current	typical : 0.05 nanoamperes maximum : 0.5 nanoamperes
spectral response	range : 185-900 nanometers peak wavelength : 420 nm.
quantum efficiency	average in the visible region : 13% at 532 nanometers : 15 %

Table 4.3. PMT Specifications

36

to reduce the RC time constant while using a 500 ohm resistor to prevent over-driving the PMT. Specifications of the preamplifier are as follows [Ref. 13] :

gain	10 fixed
output impedance	< 0.2 ohm for negative outputs
full signal bandwidth	$\geq 200 Mhz$
risetime	$\leq 2n$ sec
wideband output noise	< 50 microvolts rms
input impedance	> 1 kohm

Table 4.4. Preamplifier Specifications

The output of the preamplifier was AC coupled to a logarithmic amplifier through a mixer. This is an Analog Modules, Model 382 Logarithmic Amplifier, to amplify the weaker signals and compress the dynamic range of the return signal. Thus as the range increases the amplification by the logarithmic amplifier will increase as the signal strength decreases. The specifications of the logarithmic amplifier are given in Table 4.5. [Ref.14]

input impedance	50 ohms
input dynamic range	-200 micro V to -2 V

response	DC- 3 ns rise time,
	      fall time 5 ns to 20 dB down
	      20 ns to 40 dB down
	      40 ns to 60 dB down

output	drives 50 ohms, non-inverting
power required	+5 V and -5 V, 180 mA
connections	SMA

Table 4.5. Specifications of the Logarithmic Amplifier

A new power supply was used in this experiment due to the noise problem experienced in the previous measurements. The previous power supply in the receiver box was kept in the same place, but a new connection to the new Bertan Model 215 high

37

voltage power supply was made. The specifications of the replacement power supply are listed in the Table 4.6 [Ref.15] :

manufacturer	Bertan Associates, Inc.
output voltage	$0 to \pm 3000V$
output current	0 to 5 mA
ripple	15 mV peak-to-peak
resolution	200 mV
stability	0.01% / hr , 0.02% / 8 hr

Table 4.6. Specifications of the Power Supply

As there was no space for the new power supply on the telescope mounting it was placed adjacent to the telescope during experiments. This problem should be solved to make the overall system portable. Since the replaced power supply is still in the receiver box it may be used if the noise level at the output of the circuit can be reduced to reasonable levels. Noise is still the problem with the new power supply, probably coupling into the receiver circuitry through the power cord, acting as an antenna and receiving unwanted signal when close to any uninsulated electronic device. In particular when close to the laser transmitter box it picks up signal from the transmitted pulses; these signals (similar in shape and bigger in amplitude than the lidar signals) are observed on the oscilloscope together with the received lidar signals. Thus, the location of the power supply must be carefully examined before it is mounted on the system.

V. EXPERIMENTAL PROCEDURE AND DATA ANALYSIS

A. INTRODUCTION

The modified Naval Postgraduate School Lidar System was first tested on the basement floor of Spanagel Hall on 28 July 1995 at 16:30 hours to set the correct alignment of the laser transmitter and the receiver assemblies. The alignment was satisfied during the tests performed at a distance of 260 ft (~79.3 m). The locations of some optical elements were rearranged to increase the level of received signal. A Hewlett Packard HP 5411D Digitizing Oscilloscope which has a sampling rate of 1 gigasample per second was used during these experiments, and the received laser return signals were recorded as shown in Fig. 5.1.

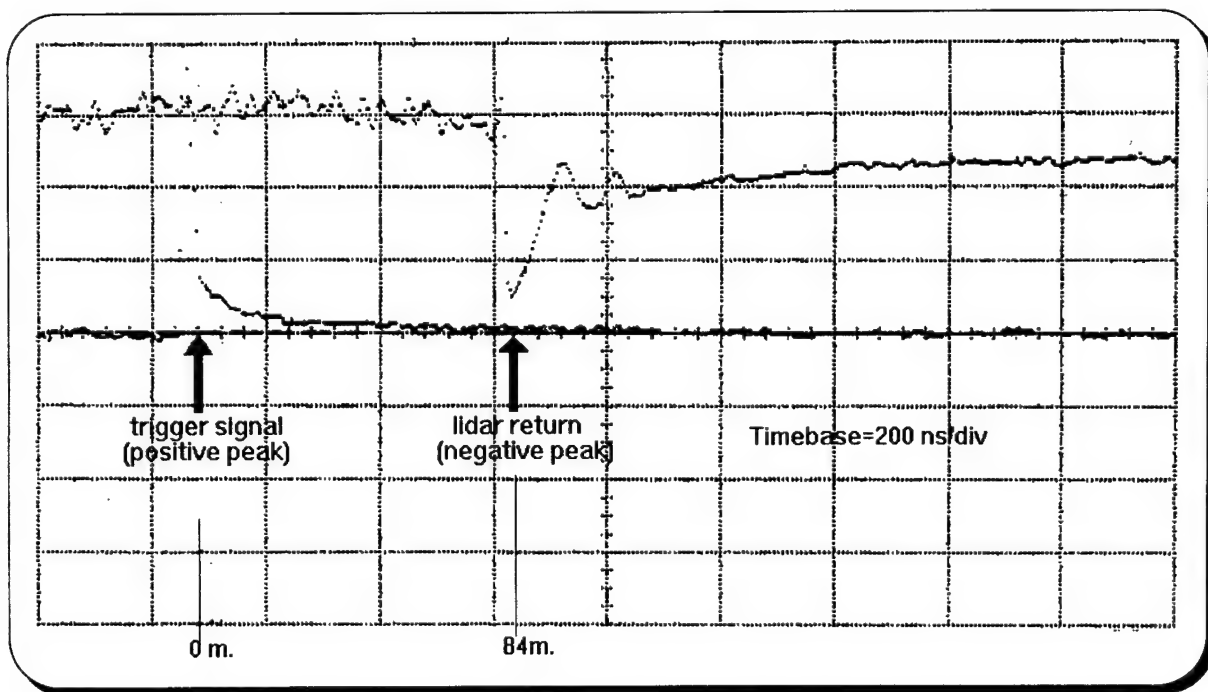Figure 5.1. Lidar Signal in Close Range Test

Experiment Setup :   Ch 1   (trigger signal)   =   500 mVolts/div

                                  Ch 2   (reflected signal)   =   200 mVolts/div

                                  Timebase   =   200 ns/div

39

The experimental data shown in Fig.5.1 and listed above shows that we have a satisfactory trigger signal level (above 2 V) and the distance measured by the time difference between trigger and receiver signals matches the real distance between the system and the reflecting plate.

After these tests the experimental equipment was carried up to the roof of Spanagel and day/night time tests started. Some of the tests were achieved using an HP 5411D oscilloscope and a Tektronix DSA 602A type oscilloscope was used later. The primary reason for switching the oscilloscope was that the latter one gave the opportunity to store the waveforms, and thus it was possible to compare the distances of reflection that were recorded at different times of the day on the same screen at a later time. The second reason to switch the device was the high sampling capability (2 gigasamples per second) of the Tektronix.

B. HARD TARGET RANGE MEASUREMENTS

To estimate the range to a hard object we must first find the cross-section area and the reflectance of the specific object which the laser beam will reflect from. For this purpose we calculate the cross-section for a circular disk model using Eq. 5.1.[Ref.2]

$$\Gamma = \pi.\rho.z^2 \tag{5.1}$$

where Γ is the laser target cross section
ρ is the reflectance of the disk's surface
z is the radius of the circular disk

Using this equation to find the hard target maximum range of our model, we can estimate the maximum range by :

$$r = \left[\frac{K.P_s.\Gamma.D^2.\eta_t.\eta_r}{4.\pi.\varphi^2.P_r} \right]^{1/4} \tag{5.2}$$

where K is the beam profile function
P_s is the transmitted power (watt)

40

Γ is the target laser cross-section (m^2)

D   is the receiver aperture diameter (meters)

η_t is the transmitter optical efficiency

η_r is the receiver optical efficiency

ϕ is the transmitter beamwidth (radians)

P_r is the received signal power (watts)

The laser in our experiment setup operates in the TEM_{00} mode as the transmitter source and this mode has a Gaussian intensity profile and for our system (for small line of sight errors) the profile of a Gaussian beam is given by:

$$K(\psi, \phi) = 2.e^{-\left(\frac{2.r^2.\psi^2}{w^2}\right)}$$ (5.3)

where ψ is the line of sight pointing error

r   is the range to the target

w   is the beam radius

We can estimate the performance of our radar by making some approximations and substituting the specifications of our system into the Eq. 5.1, 2, 3 as:

-The reflection coefficient is 0.10 for a long needle pine. [Ref.16]

-The target radius is 1 meter

-The pointing error is 1.52 milliradians (declination angle between the laser and receiver axis)

-The receiver optical efficiency is 0.38

-The transmitter optical efficiency is 0.66

-The beam profile function value is 4.[Ref.17] (Since the entire Gaussian profile is within the receiver FOV we can assume the uniform profile with K=4)

We made assumptions for the values of the reflectance, radius of the circular disk, beam profile function. We assumed that the reflections are from long needle pines that are very common in our terrain. The second assumption is the physical shape of the target. We assume that it is a circular disk with radius of 1 meter.

These parameters were substituted into Eq. 5.2 which yielded the theoretical maximum range of 3172 meters. To test this estimate the system was tested on hard targets. The reflection signals from the trees are recorded as in Fig. 5.2 and Fig.5.3.
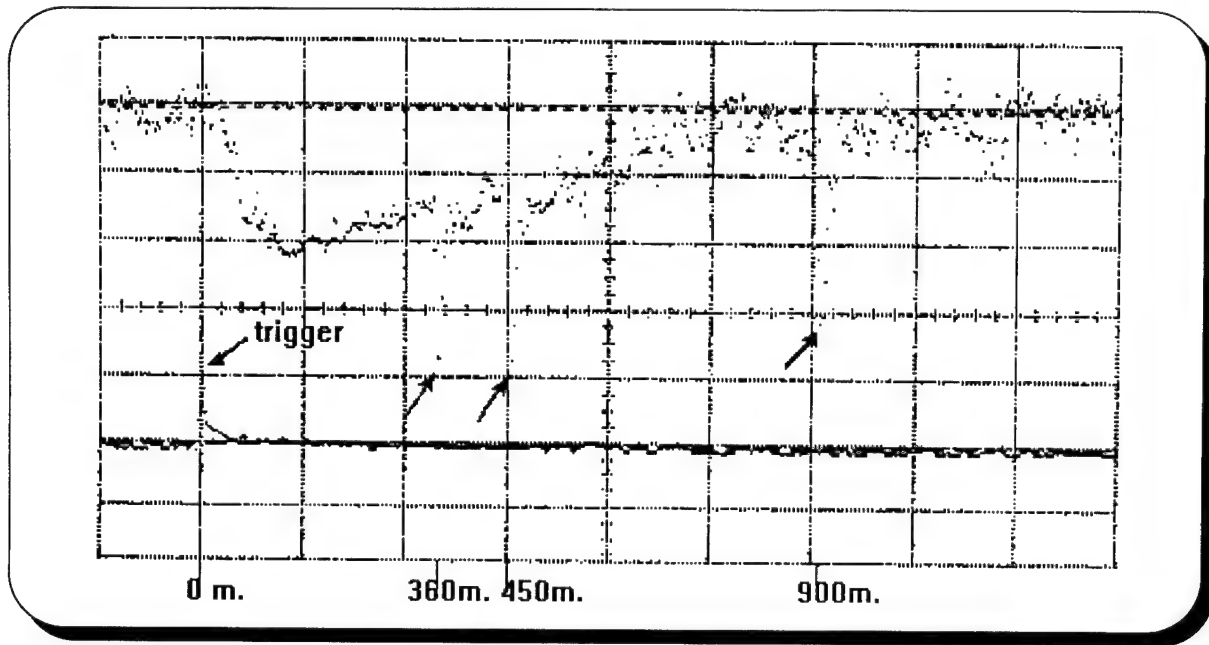

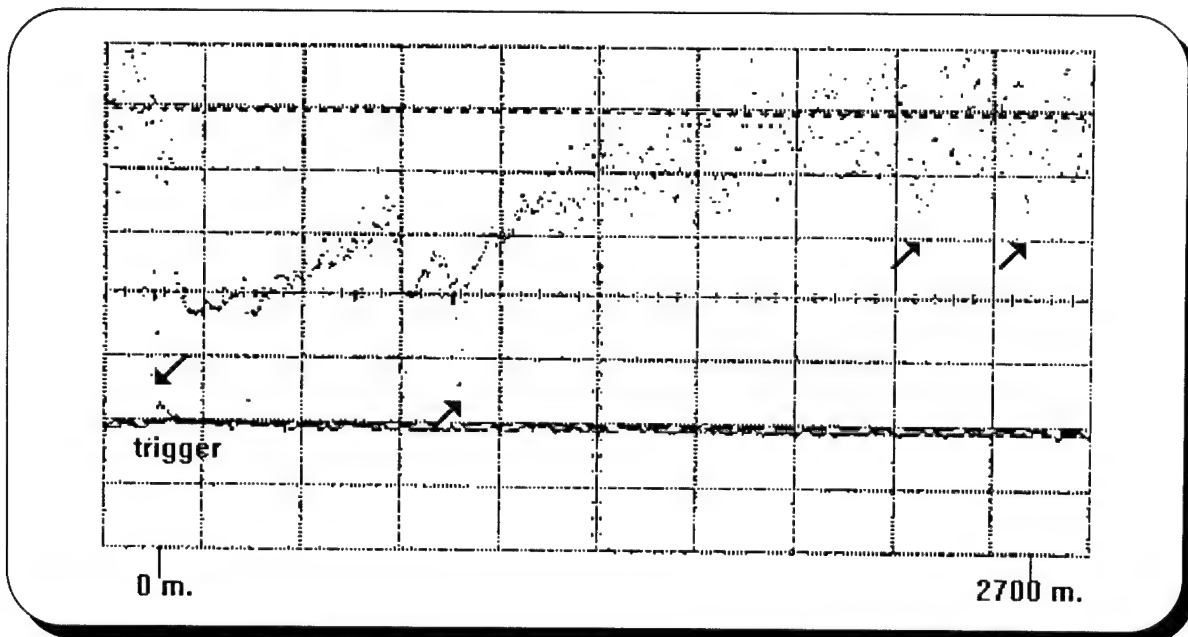Figure 5.2. Lidar Returns Showing Hard (Tree) Targets at 340m, 450m and 900m.

Figure 5.3. Lidar Returns Showing Hard Targets at 900m, 2400m and 2700m

42

In Fig. 5.2 the high voltage power supply level is 750 V. We have three separate returns from trees at ranges 360 m, 450 m, 900 m. The scale of the figure is 1 microsecond/div. In Fig.5.3 the high voltage power supply level is 800 V and scale is 2 microseconds/div. We have returns from trees at different ranges (maximum at 2700 m). Since the noise grows with the amplifying voltage we couldn't increase the range beyond 3500 meters during daytime experiments. However, we reached a range over 5000m during night time measurements since the background noise was no longer a problem. The daytime range of the lidar system can be increased by applying a pinhole filter before the fiber optic cable and after the narrow band filters. Changing the PMT-which is very noisy- in usage now is expected to contribute to expanding the range limits of the system.

C. MEASUREMENT OF ANOMALOUS PROPAGATION CONDITIONS

We can find the theoretical atmosphere return range for daytime operation from Eq. 3.13. We use the following parameters of our system in this equation:

P_0 (the transmitted power) $= 0.203 \times 10^6$ watts
τ (laser pulse width) $= 45$ nanoseconds
$\beta(r)$ (atmospheric volume backscattering coeff. at range "r") $= 1 \times 10^{-5}$ (average value)
c (speed of light) $= 3 \times 10^8$ m
A_0 (effective aperture of the receiver) $= 0.0285$ m^2
λ (wavelength of the background) $= 532$ nanometers (centered at the same wavelength
    as the laser beam because of the 532 nm/.8nm filters used)
$\eta(\lambda)$ (quantum efficiency of the PMT) $= 0.15$
$\sigma(r)$ (atmospheric attenuation coefficient) $= 5 \times 10^{-4}$ (average value)
h (Planck's constant) $= 6.626 \times 10^{-34}$ watts. sec^2
$\Delta\lambda$ (narrow band filter bandwidth) $= 0.8$ nm.
$S_b(\lambda)$ (spectral radiance of the background) $= 0.15$ watts.meters^{-2}.str^{-1}.micron^{-1}
$\tau_0(\lambda)$ (receiver optic transmission efficiency) $= 0.38$
Ω_0 (receiver solid angle) $= 7.52$ milliradians
Δf (receiver bandwidth) $= 1.250 \times 10^9$ hertz

Inserting these parameters into the day time range equation (Eq.3.13), then we find;

$$r_{max} = 39786 \cdot e^{-[5 \times 10^{-4} \cdot r_{max}]}$$

and solving this equation we find the day time maximum range as 4403 meters.

We can estimate the night time range by substituting the same parameters into Eq. 3.17 and solving the equation as in the above process; we find a value of 8013 meters.

In order to make comparison to the radiosonde balloon data the radiosonde launch results were taken from a concurrent shipboard launch in the Monterey Bay Area. Most of the tests are done within a range of 20 to 30 miles from Monterey. The results in these boundary layer plots can be assumed valid for our test area. The boundary layer data taken for three days on the ship are shown in Figs. 5.4/5/6/7/8. These figures will be compared to the results that were obtained from the lidar experiments that we executed.
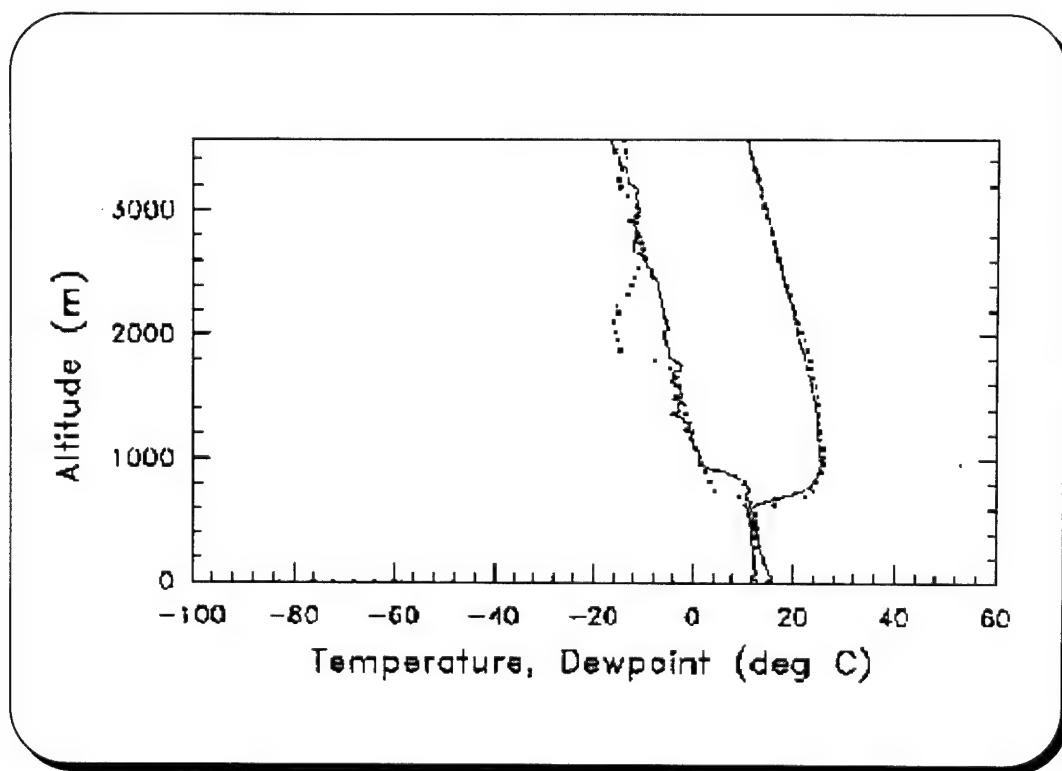

Figure 5.4. Radiosonde Profiles of Temperature and Dewpoint

Date and Time = 4 Aug 95   13:28 (Monterey)

Location   = 36.33 N   122.15 W
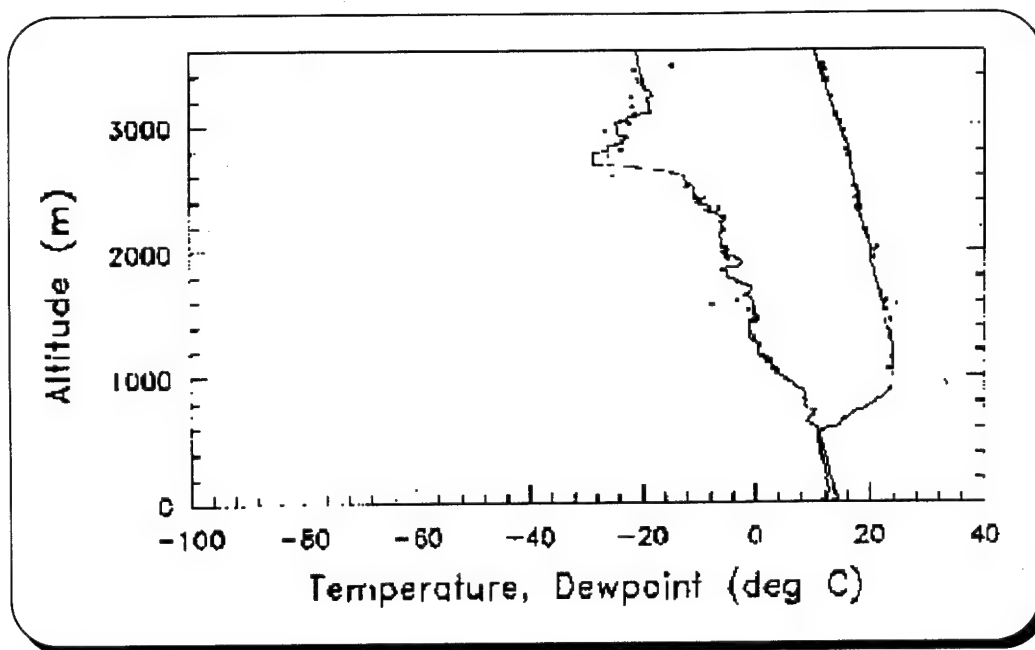
Boundary Layer Height $\cong$ 600 m.

Figure 5.5. Radiosonde Profiles of Temperature and Dewpoint

Date and Time = 5 Aug 95   00:36 (Monterey)   Location   = 36.75 N   122.03 W
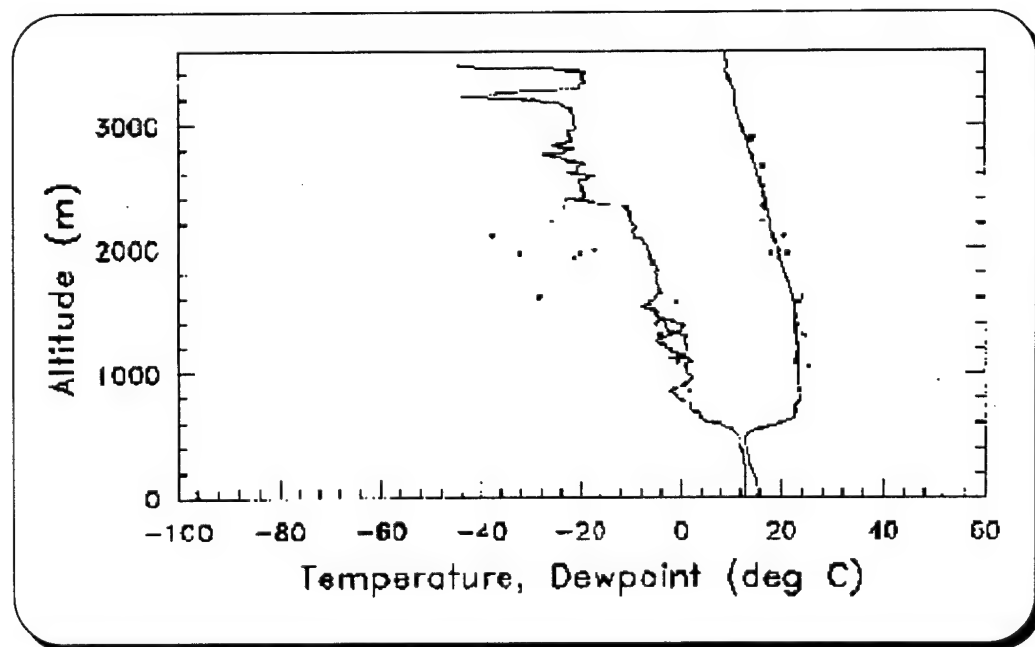Boundary Layer Height ≅ 600 m.

Figure 5.6. Radiosonde Profiles of Temperature and Dewpoint

Date and Time = 5 Aug 95   17:54 (Monterey)   Location   = 36.74 N   122.01 W
Boundary Layer Height = 500 m
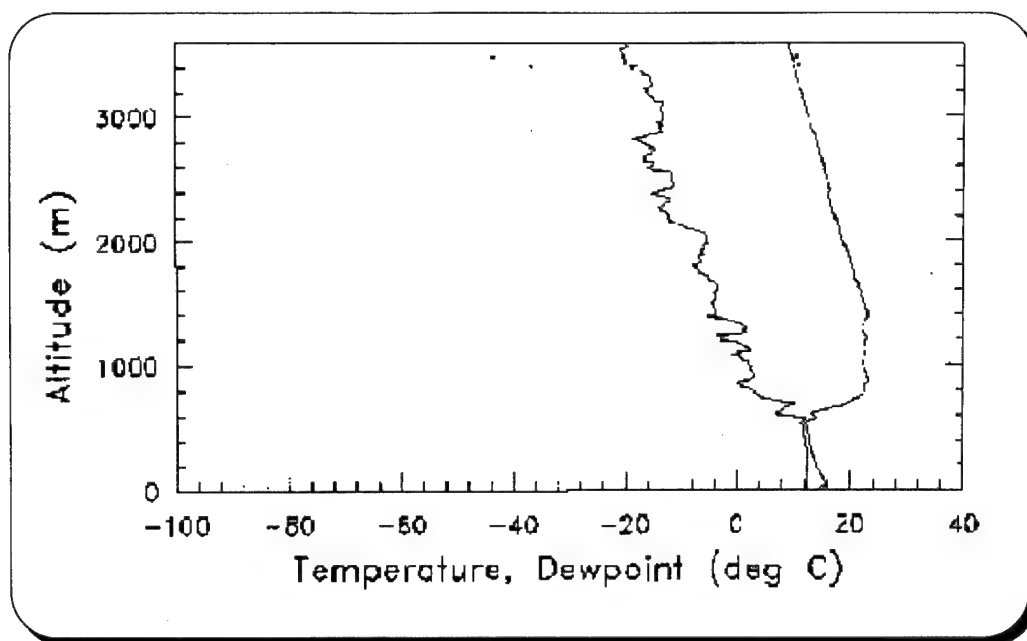
45

Figure 5.7. Radiosonde Profiles of Temperature and Dewpoint

Date and Time = 5 Aug 95   21:57 (Monterey)   Location   = 36.75 N   122.03 W

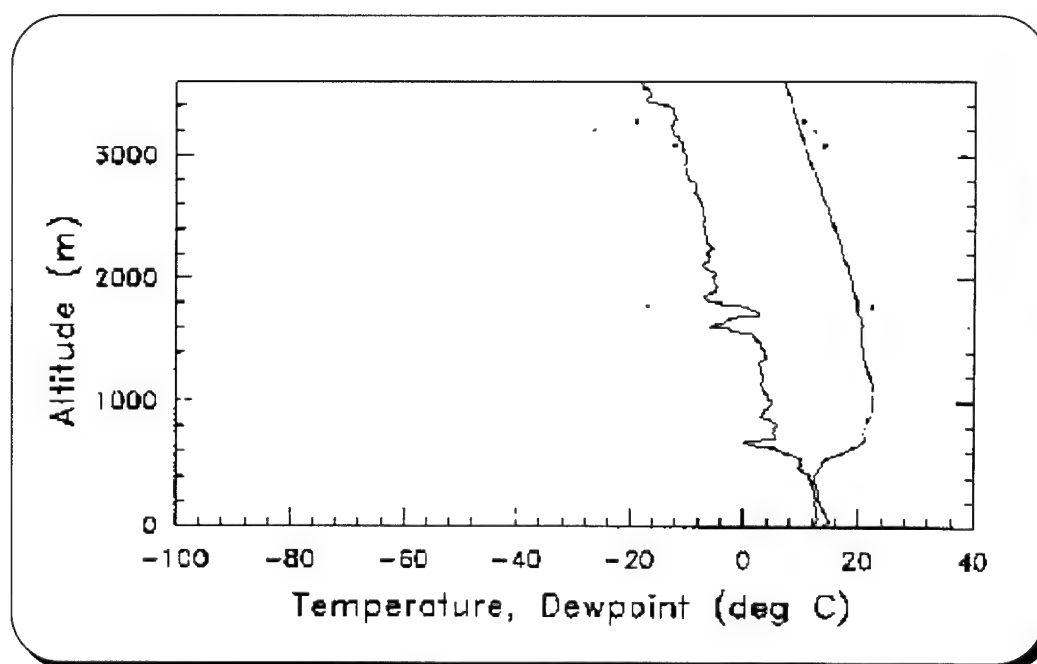Boundary Layer Height = 550 m

Figure 5.8. Radiosonde Profiles of Temperature and Dewpoint

Date and Time = 6 Aug 95   19:25 (Monterey)   Location   = 37.39 N   123.09W

Boundary Layer Height = 400 m

The radiosonde launches above show the boundary layer height for three days/nights; 4, 5, 6 August. The height where the temperature isograph starts to increase and the dewpoint isograph starts to decrease very rapidly is the altitude at which the boundary layer ends. The boundary layer height at those specific times did not show great contrast to usual daytime values except during early morning times. Since the boundary layer came close to the ground at this time of the day, there is no value to show in these graphs here for observing correlation between lidar measurements and radiosonde launches.

The lidar experiments achieved on the days 3 to 5 August gave the following results (Fig.5.9, 10,11) for the day and night reflection ranges:
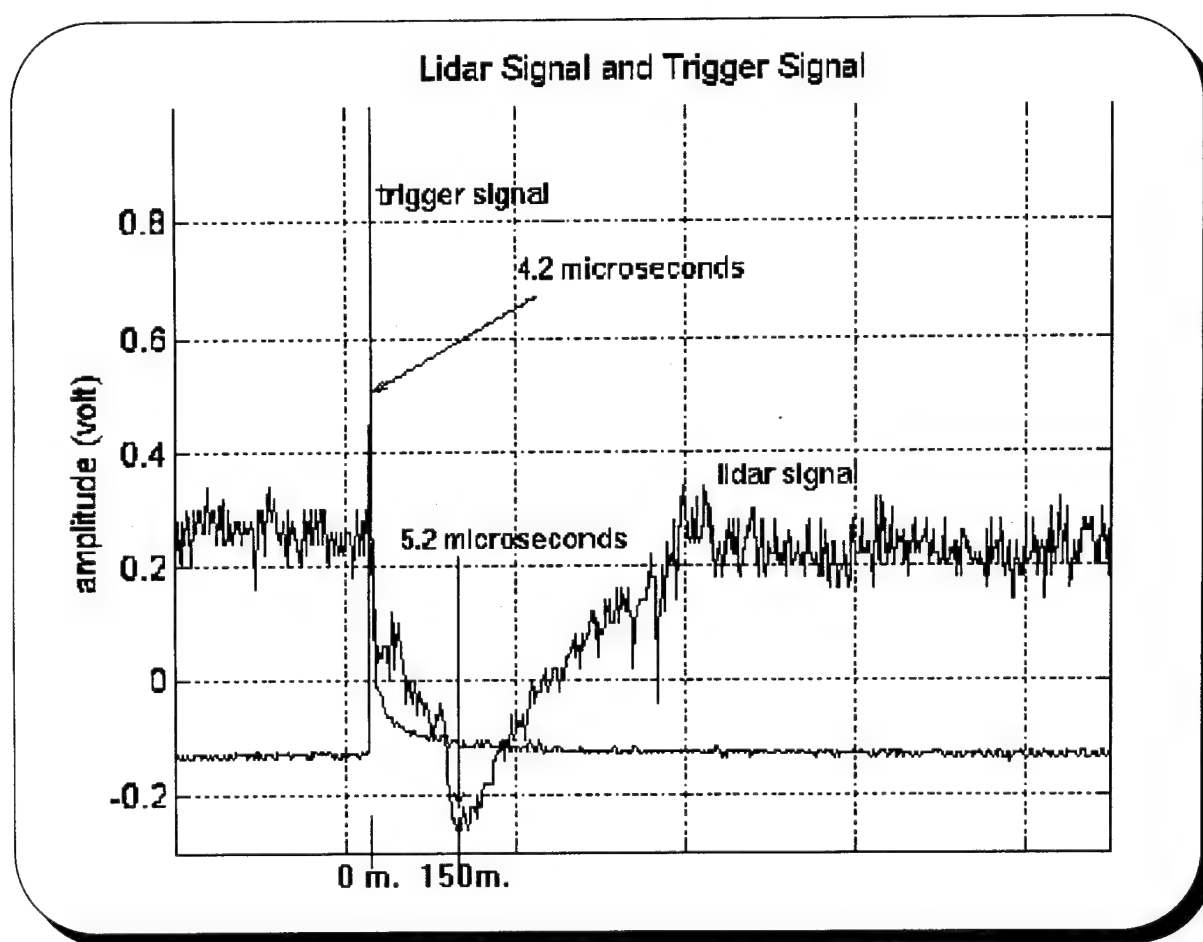

Figure 5.9. Night Time Lidar Return Signal from Haze Layer (Platform elevation is 30 m)

Date, Time = 3 Aug 95   22:13 (Monterey)   Weather Condition : Thick layer of haze

47

The reflection signal in Fig.5.9 above is 1 microseconds after the laser pulse transmitted and the platform is about 30 m above the ground. So the reflection is from 180 meters altitude. The laser beam is expected to be reflected from the layer of haze which existed at the time of experiment. So this reflection does not give any idea about the boundary layer at that time but shows the occurence of haze which is the sign of condensed water vapor.

The second experiment was performed in the night of 4 August 95. The reflections are recorded as in Fig.5.10.
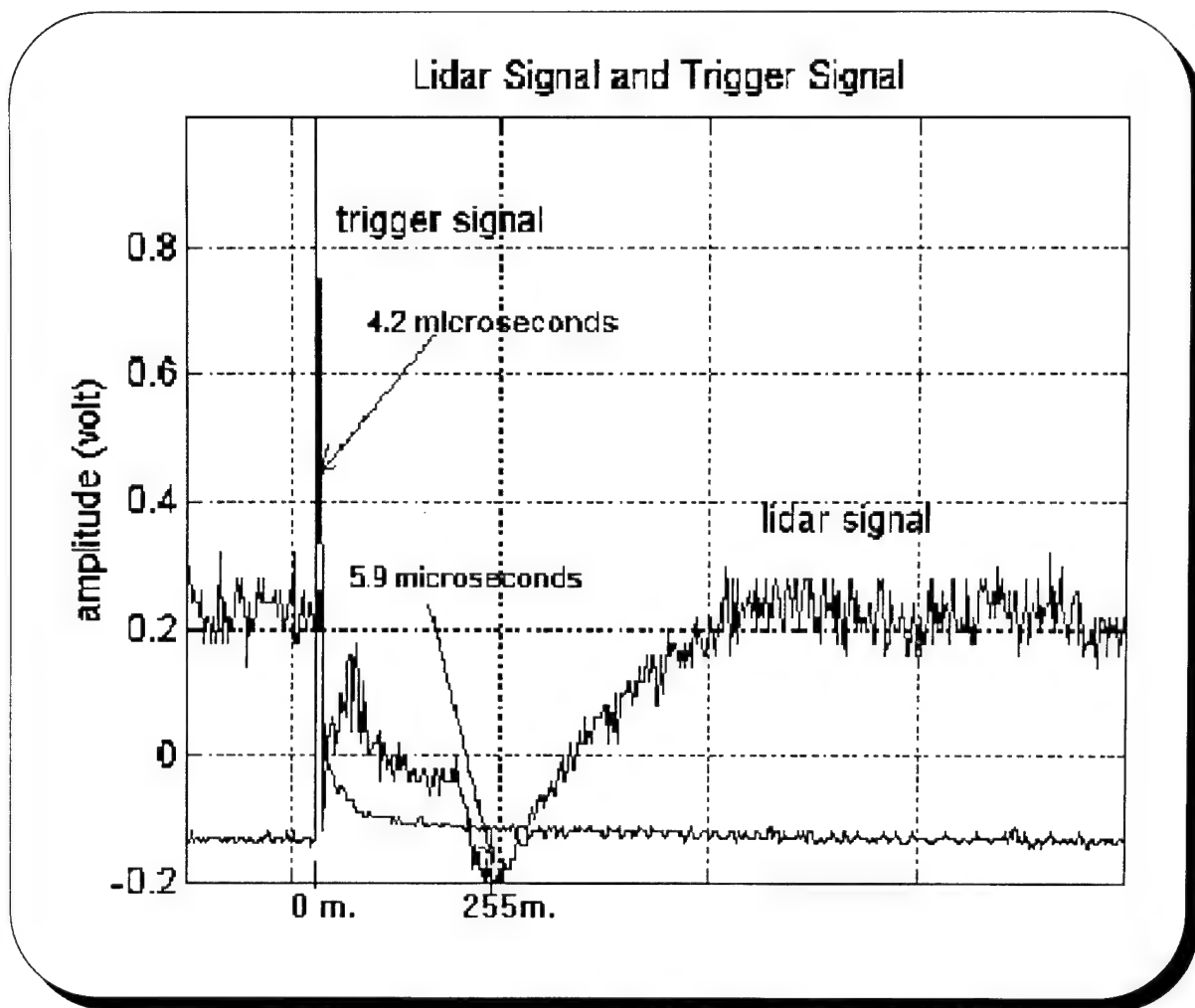

Figure 5.10. Night Time Lidar Return Signal from Haze Layer (Platform elevation is 30 m)

Date, Time = 4Aug 95 22:00 (Monterey)   Weather Condition : Thin layer of haze

48

The signals received in this experiment were not from the boundary layer either. It is clear in Fig. 5.4 and Fig.5.5 (we take the average of them to estimate the layer height at 22:00) that the boundary layer height during these experiments was about 600 meters in the Monterey Bay Area close to Monterey. Even though the haze was not as dense as it was in the previous night, we got the reflections from the floor of the haze. The time difference between the trigger signal and the received lidar signal in Fig. 5.10 is 1.7 microseconds which corresponds to an altitude of 285 meters (including the platform height).

The daytime experiments performed on 5 August 95 yielded Fig. 5.11.
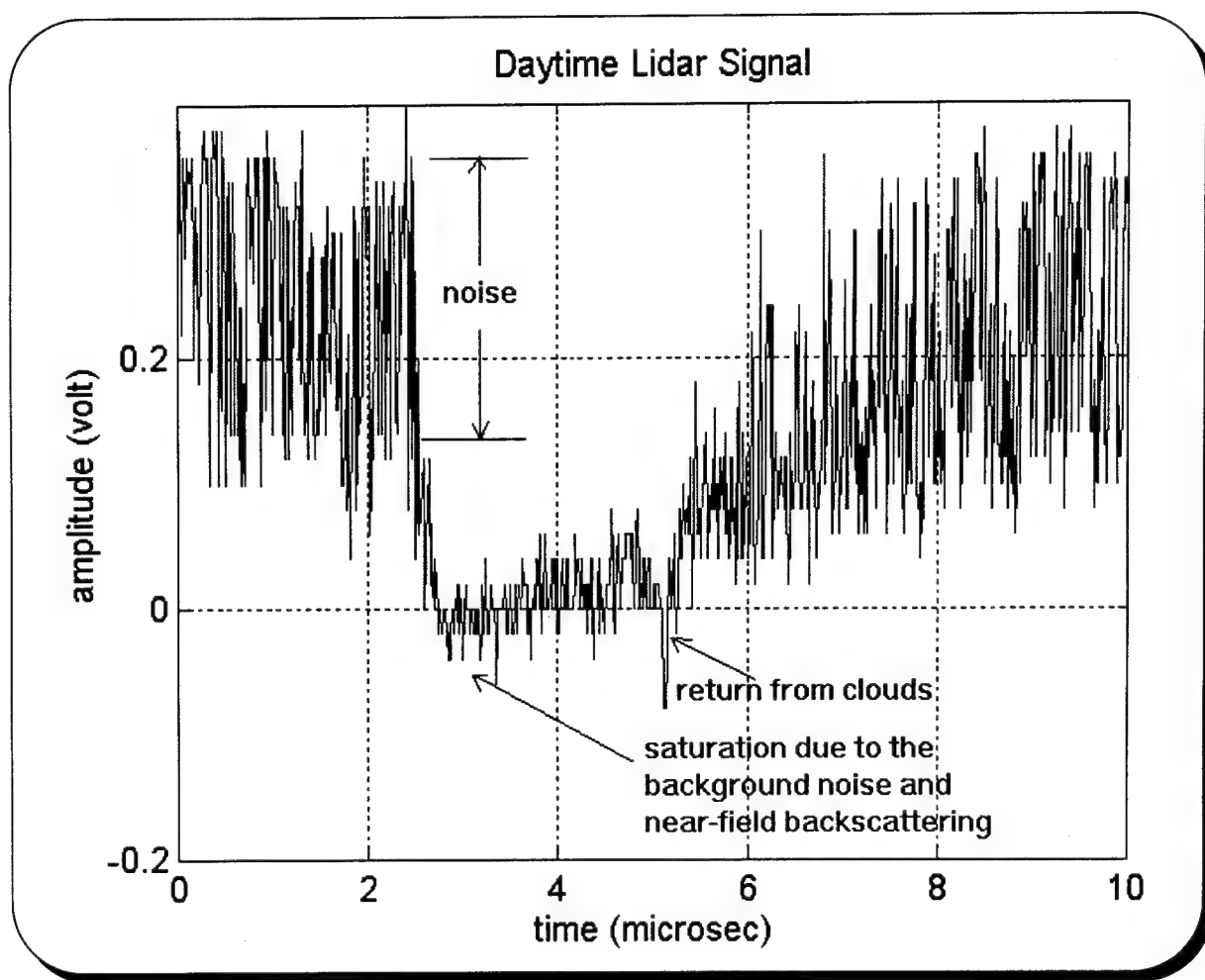

Figure 5.11. Daytime Lidar Return

Date, Time = 5 Aug 95   18:00 (Monterey)   Weather condition : scattered cumulus clouds

Figure 5.11 gives us the floor height of the cumulus clouds (which is an anomalous propagation condition) that existed at the time of boundary layer measurements. The significant point in this figure is the level of noise. It is about 0.2 volts peak-to-peak. This noise is due to the background that originates from solar radiation. Despite the filters used, the wide angular field-of-view increased the level of background noise. Since we took the output from the logarithmic amplifier, what we see is the amplified noise through the PMT and logarithmic amplifier. We kept the high voltage power supply level below 700 volts during the daytime measurements to prevent the PMT being damaged by the amplified background signal. The voltage for the night time measurements was changed from 700 volts to 1900 volts.
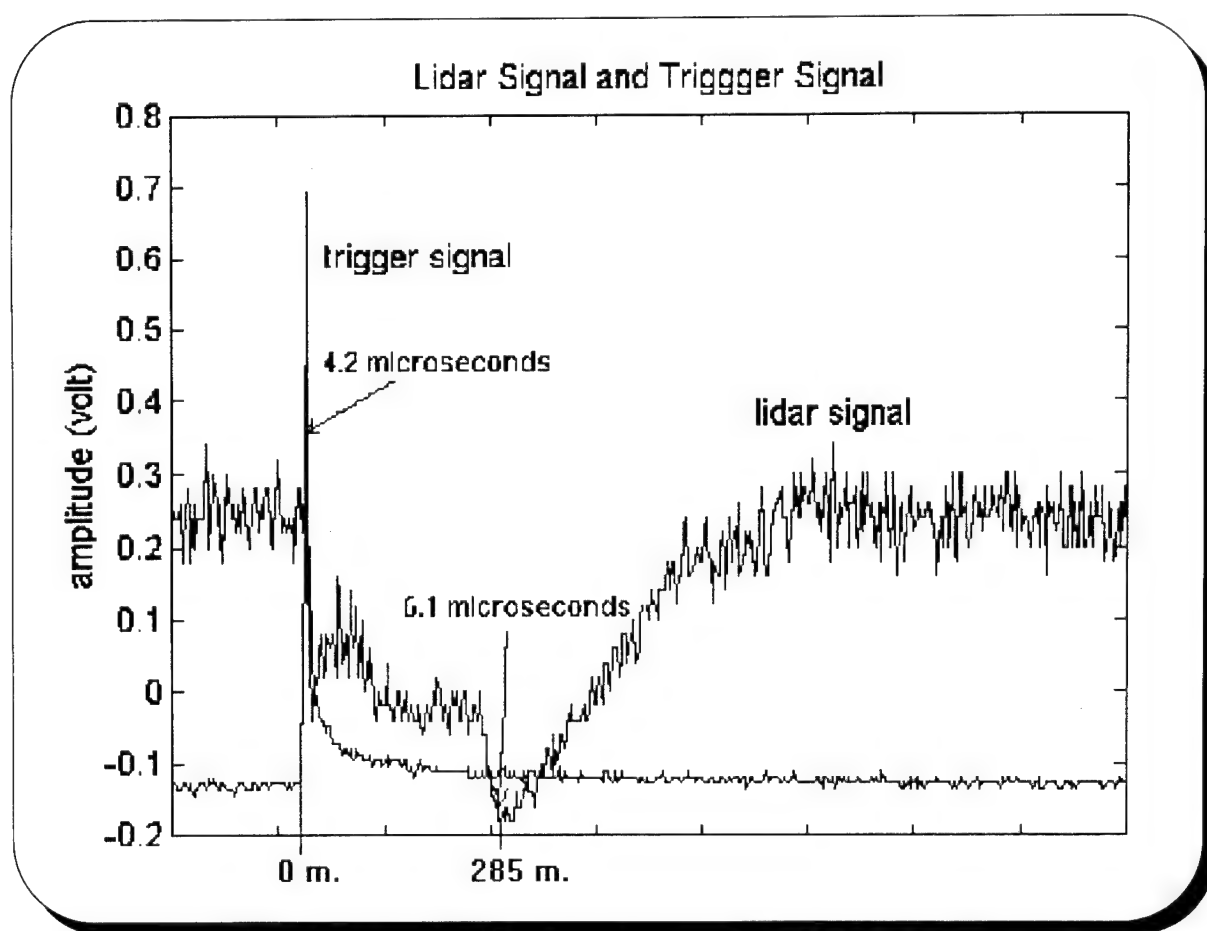

Figure 5.12. Night Time Lidar Return Signal from Clouds

Date, Time = 5 Aug 95   21:00(Monterey)   Weather condition = scattered cumulus clouds

50

The reflection in Fig. 5.12 is from the clouds at about 315 meters altitude. The radiosonde balloon measurements made at this time showed a boundary layer height of 550 m. Since this is well above the strongly reflecting surface-clouds- in our lidar experiment we could not reach to the boundary layer altitude.

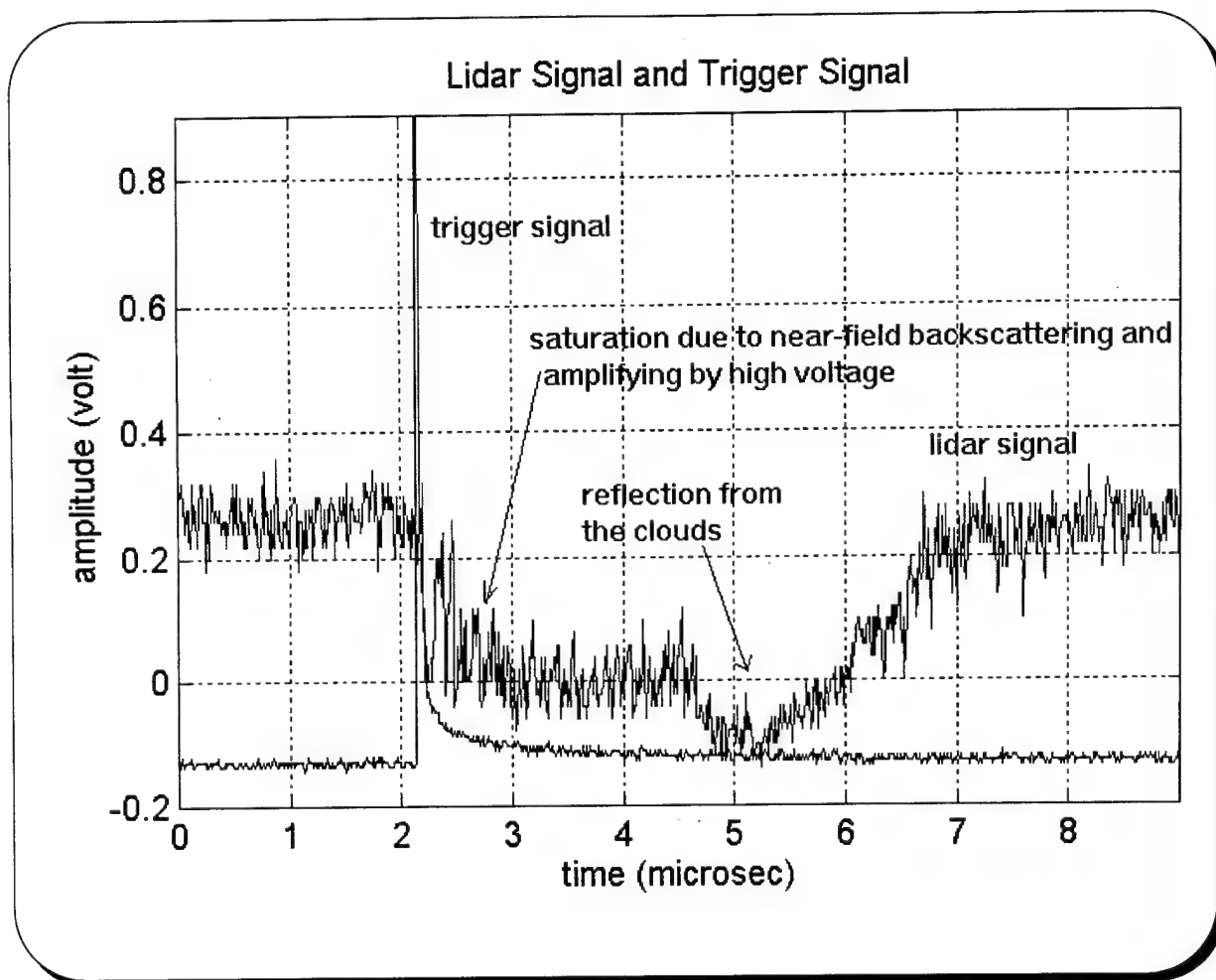Figure 5.13. Night Time Lidar Return with Cloud. PMT Showing Deterioration.

Date, Time = 6 Aug 95   22:00(Monterey)   Weather conditions = cloudy

Figure 5.15 represents a night shot on the following day. The first wide, downwards peak in Fig. 5.13 is due to the nearfield backscattered radiation saturating the photomultiplier. Even though the experiment was executed at night, due to the degraded performance of the PMT we

had to use high voltage levels to amplify the receiver part to get clear signals. The distance between the trigger and this first peak is stable in most of the high voltage amplifying or high background noise cases because of the near-field backscattering. This range varies between 60 to 80 meters. The second peak hardly noticeable in the main peak (5 microseconds away from the trigger signal) is believed to give the boundary layer height. But, it is not certain in the above case that the reflection is from the boundary layer ceiling since at the time of the experiment it was heavily cloudy and we did not know the altitude of the clouds. The experiments performed in the night of 6th August and the days after this yielded weak lidar returns that are hidden by the strong electronic noise due to the degraded PMT performance. The data during these experiments was collected with the Tektronix, DSA602 Digitizing Signal Analyzer and recorded in ASCII code to be processed later.

The lidar system went out of operation on 8th of August because of breakdown of the PMT. The data processing was done with the already existing lidar measurements and comparison with the radiosonde launch data was made later. The conclusions drawn from these comparisons and the data processing is described in Chapter VI. Recommendations to increase the system performance are given there also.

VI. CONCLUSION AND RECOMMENDATIONS

The Naval Postgraduate School Lidar System was modified to give better results than in the previous years to compare with the radiosonde launches. The modification in the transmitter system includes change of the transmitter telescope and modifications of the optic elements in the laser box. Modification in the receiver system includes the change of the receiver telescope, the power supply and the connection elements between the receiver telescope and the photomultiplier box. These changes yielded a higher beam power density and uniformity at the end of the transmitter telescope, satisfactory received signal level at the output of the receiver telescope, less noise (due to the power supply) at the signal analysing stage.

The relocation process of the transmitter and receiver telescopes relative to each other yielded a range of 50.13 m. for the beginning of overlap. Since no reflection signal was expected during the experiments under this range it was short enough. Preventing short range overlapping also helps reduce the near-field backscattering significantly. The new mounting of the telescopes allowed the system to be tilted higher in elevation (to 90 degree elevation).

The modification of the optic elements in the transmitter box includes correcting the input alignment of the laser head and the optics, changing the mirror system at the rear output of the laser head, and relocating the optics. Changing the height of the optics caused more laser energy to enter the telescope by improving alignment. Changing the mirror system facing the rear end of the laser system yielded a high level stable trigger signal. Changing the location of the optics in the transmitter system yielded a better collimation of the laser beam before it enters the transmitter telescope and a uniform beam at the output of it.

The modification of the receiver system elements started with the change of the receiver telescope. The new telescope has a larger optical aperture compared to the previous one. The second step was the coupling of the receiver telescope output to the photomultiplier tube which was located in the transmitter box through a fiber optic cable instead of direct coupling via a metal pipe as in the previous system. This allowed more complicated optical setups to be tested in the pipe without harming them and without detaching all the receiver system. The third step was changing the power supply which decreased the noise level in the amplified signal significantly. The previous power supply was kept in the receiver box due to a probable future

requirement for decreasing the noise signal originating from it and using it again. The last step was the tests for the endurance and the noise level of the cable connecting the high voltage power supply to the photomultiplier tube. It was found that some random spikes in the amplified signal occurred above about 800 volts and that disturbances increased rapidly as the voltage increased. So the connecting cables were changed and the problem was eliminated.

After all these modifications, we got very clear returns from ranges above3000 meters for night time measurements and above 1500 meters for daytime measurements. Since the radiosonde launch data we have belong to the days when it was not clear enough in Monterey, we could not decide whether the returns were from clouds, haze or the boundary layer itself. But the system gave clear signals in the case of anomalous propagation conditions such as heavily or scattered clouds, haze, fog, etc. which causes the reflection of the radio wave signals and range/angular error of them.

To increase the sensitivity of the system to the boundary layer signals and to make valuable comparison of radiosonde data and lidar data, further modifications on the system must include:

1. The trigger signal cable (the fiber optic cable transferring the laser signal from the rear end of the laser head to the pin diode) must be changed due to the deformation of the cable. It was found that the cable was not tight enough in its connection to the pindiode input, and that sharp bends in the cable in some locations may result in a lower trigger signal level. Even though the trigger signal in the current system is high enough to trigger the analysing system, the elimination of this problem will probably give a firm high voltage level.

2. The laser output is significantly reduced by the end of the experiments and it does not fire regularly in each triggering. The firing interval increased significantly compared to the previous experiment; it became over four seconds in average. The laser needs to be sent back to the manufacturer for reconditioning.

3. The transmitter efficiency must be recalculated for the new experiments.

4. In case of changing the collimation adjustment of the transmitter telescope, it must be shown first that the modified beam is not converging. These tests can be achieved in the basement floor of Spanagel which has a clear range of enough length (over 100 m.).

5. The inclination angle between the transmitter and receiver telescopes must be adjusted with a more stable and controlable setup. The adjustment made in our system is feeding the gaps with small metal sheets that aligned the two system according to each other. What can be made is putting an adjustment system to the mounting of the receiver telescope which allows it to be tilted ± 2 mrad. in azimuth and in elevation.

6. Background noise is still a big problem which limits the daytime (time when the boundary layer is more observable) measurements and hides the weak signals coming from long ranges or from less dense media. Since the solar spectrum reaches to its peak values during daytime measurements, extra filtering must be applied to the system. It might consist of some additional narrow band filters and a pinhole before the fiber optic cable.

7. The photo multiplier tube (PMT) showed deterioration at the end of the experiments and it should be changed. The new PMT should have higher gain (more than 3×10^3) and low anode dark current.

8. Noise generated by the circuit elements must be examined again. The voltage source feeding the electronic circuits is probably one of the significant noise sources.

9. The previous power supply might be examined and used after the noise at the output of it is filtered or additional shielding added.

10. The new high voltage power supply (HVPS) must be mounted on the system to make it more compatible. The new location of the HVPS must be chosen so that it does not increase the noise level in the processed signal.

11. The 6×30 finderscope must be aligned with the receiver telescope to enable easier adjustment of the transmitter and receiver fields of view.

12. The procedure for comparison with radiosonde data must be evaluated. Since the weather conditions and layer heights do not change over short distances, the radiosonde data from any experiment in the Monterey Bay Area can be used to medium accuracy.

The Naval Postgraduate School Lidar System is capable of measuring many of the anomalous propagation conditions at a satisfactory level and probable boundary layer heights with moderate accuracy. Better results are expected after the problems described above have been eliminated. It can be said that the results from the lidar experiments are satisfactory on the basis of the detected signals and their ranges, which also shows that the goal of the thesis is reached to large extent.

LIST OF REFERENCES

1. Regush, M.M., *Development of a LIDAR for Integration with the Naval Postgraduate School Infrared Search and Target Designation (NPS-IRSTD) System*, Master's Thesis, Naval Postgraduate School, Monterey, California, June 1993.

2. Mallo, G., *Modification of The Naval Postgraduate School Lidar System*, Master's Thesis, Naval Postgraduate School, Monterey, California, September 1994.

3. Eaves, J.E. and Reedy E.R. , *Principles of Modern Radar*, pp.51-55, New York City, New York, 1987.

4. Bean, B.R. and Dutton, E.J., "Tropospheric Refractivity" in *Radio Meteorology*, pp.49-88, U.S. Government Printing Office, Washington D.C., 1966.

5. Nathanson, "Tropospheric Refraction Effects" in *Radar Design Principles*, pp.218-220, Mc Graw-Hill Book Company, New York City, New York, 1969.

6. Davidson, K., Lecture notes from MR 2416, Meteorology for Electronic Warfare.

7. Bean, B.R and Dutton, E.J. "N Climatology" in *Radio Meteorology*, pp. 149, U.S. Government Printing Office, Washington D.C., 1966.

8. Measures, R.M., "Laser Systems as Remote Sensors" in *Laser Remote Sensing Fundamentals and Applications*, pp. 205-236, Krieger Publishing Company, Malabar, Florida, 1992.

9. Cooper, A.W. Lecture notes from PH 3208, *Electro-Optic Principles and Devices,* Naval Postgraduate School, Monterey, California, 1994

10. Measures, R.M., "Laser Remote Sensor Equations" in *Laser Remote Sensing Fundamentals and Applications*, pp. 237-280, Krieger Publishing Company, Malabar, Florida, 1992.

11. Celestron Corporation, Model C14 Telescope User's Manual.

12. Hamamatsu Corporation, Photomultiplier Tube Catalog, 1990.

13. Le Croy Corporation, Model VV100B Wideband Pulse Amplifier Specifications, June 1988.

14. Analog Modules Inc., Model 382 Logarithmic Amplifier Specifications, February 1994.

15. Bertan Associates, Model 215 High Voltage Power Supply User's Manual.

16. Decker, W.M., *Measurement of Reflectivity*, United States Military Academy, West Point, New York, 1987.

17. Kamerman, G.W., "Laser Radar" in *The Infrared and Electro-Optical Systems Handbook*, pp.2-35, v.6, SPIE Optical Engineering Press, Bellingham, Washington, 1993.

INITIAL DISTRIBUTION LIST

1. Defense Technical Information Center..2
Cameron Station
Alexandria, VA 22304-6145

2. Library, Code 52...2
Naval Postgraduate School
Monterey, CA 93943-5101

3. Chairman, Code EW..1
Electronic Warfare
Naval Postgraduate School
Monterey, CA 93943

4. Professor A.W. Cooper, Code PH/Cr...1
Department of Physics
Naval Postgraduate School
Monterey, CA 93943

5. Mr. W. Lentz, Code PH/Lz..1
Department of Physics
Naval Postgraduate School
Monterey, CA 93943

6. Professor K. Davidson, Code MR/Ds...1
Department of Meteorology
Naval Postgraduate School
Monterey, CA 93943

7. Commander, Naval Sea Systems Command..1
AEGIS Program Office
PMS-400B ATTN: CDR J.W.Wilson
2531 Jefferson Davis Hwy
Arlington, VA 22242-5165

8. Commander, Naval Sea Systems Command..1
Program Executive Officer-Theater Air Defense
ATTN: Mr. J.E. Misanin
2531 Jefferson Davis Hwy
Arlington, VA 22242-5170